



Visual Processing of Motion Boundaries

W. L. SACHTLER,* QASIM ZAIDI†

Received 20 December 1993; in revised form 8 June 1994

Psychometric functions for motion detection were measured for various spatial velocity profiles made of independently moving lines of random dots. In the first experiment, sensitivity was greater for square-wave velocity profiles than for sine waves of the same fundamental spatial frequency. Sensitivity for square waves depended on the phase of the waveform with respect to the fixation point, which precludes a characterization of the processes underlying the detection of shearing motion as a translation-invariant system. The second experiment, using velocity fields created by spatial superposition of sine waves, showed that motion boundaries facilitate detection of motion due to the steepness of the velocity gradient, and not simply because of added power at higher harmonics. In the third experiment, fluted velocity waveforms were created by subtracting the fundamental sinusoidal component from square waves, retaining sharp motion boundaries between opposing directions but removing the regions of uniform motion. Subtracting the fundamental from low-frequency square waves did not lower sensitivity to motion, indicating that sensitivity was largely determined by the presence of motion boundaries. In the final section of this article, a model is presented that can account for the data by using linear center-surround velocity mechanisms whose sizes increase with eccentricity while their sensitivity for shearing motion decreases.

Motion boundaries Velocity gradients Optic flow field Segmentation Motion sensors

INTRODUCTION

To function effectively in the real world, an observer must segregate different objects from each other and from the background, estimate their position, distance, and direction and velocity of motion. A number of visual cues, such as luminance, color, shading, texture, shape, and disparity, facilitate this task. A particularly useful source of information is the image flow field, which assigns to each point in the visual field a two-dimensional velocity vector that is the projection of the instantaneous three-dimensional velocity of the corresponding point in the scene. For example, Kaplan (1969) and Rogers and Graharn (1979) showed that observers could derive an estimate of the three-dimensional layout of a scene from the image flow field alone when shape and shading information were minimized by using random-dot fields. This derivation must take account of the fact that velocity fields in the real world do not have a simple structure: some regions in a dynamic scene consist of fairly uniform velocities separated by a sharp change in velocity, as at the boundaries of flat objects moving in front of a stationary background, while other regions have smooth velocity gradients, as for a rigid rotating cylinder. In addition, different parts of moving

objects also move relative to one another as well as partially occlude each other, like a runner's limbs and torso. We were interested in determining if there exist processes that simplify the extraction of spatial information from the velocity fields created on the retina. In particular, mechanisms providing an enhanced sensitivity to velocity discontinuities could be used to segregate an object from the background and outline its shape. In this paper we present experiments and a model concerning sensitivity to image flow discontinuities.

Image flow has been analyzed extensively in the machine and human vision literature. The major effort has gone into methods of estimating the image flow field from image sequences, such as feature matching (e.g. Ullman, 1979), correlations (e.g. Reichardt, 1961), spatio-temporal gradients (e.g. Horn & Schunck, 1981), and spatio-temporal energy (e.g. Adelson & Bergen, 1985; van Santen & Sperling, 1985; Watson & Ahumada, 1985). In this study we were interested in the kinds of operations that can be performed once the flow field has been extracted from a scene. For example, when an observer is in motion, the relative velocities of different parts of a scene are transformed roughly proportional to the distance from the observer in certain cases, i.e. motion parallax (Helmholtz, 1925). These relative velocities can be used to estimate the relative positions of objects in dynamic scenes. In addition, differential calculations on a continuous velocity field can be used to extract slant and curvature of surfaces (Koenderink & van Doorn, 1975, 1976, 1992; Longuet-Higgins &

*Department of Psychology, Columbia University, New York, NY 10027, U.S.A.

†Vision Research Laboratory, The Lighthouse Research Institute, 111 East 59th Street, New York, NY 10022, U.S.A. [Email qz@paradox.psych.columbia.edu].

Prazdny, 1980; Hoffman, 1982). Surprisingly, a prominent aspect of flow fields that has generally been neglected is the location of velocity discontinuities. In fact, many algorithms employed in machine vision tend to blur the boundaries of moving objects to facilitate computations requiring continuity (Fennema & Thompson, 1979; Horn & Schunck, 1981; Bergen, Burt, Hingorani & Peleg, 1990). This process degrades information about the shapes of objects.

A few computational studies have explicitly demonstrated the utility of velocity discontinuities. Nesi (1993) exploited variational calculus methods that explicitly keep track of discontinuities (Mumford & Shah, 1989) to retain velocity discontinuities in the estimated optical flow. This method helped maintain sharp outlines of moving objects in the flow field and thus facilitated shape extraction from image sequences. Singh and Allen (1992) showed that an estimation-theoretic framework based on local neighborhoods that retains information about motion boundaries in optic flow fields allows a more precise calculation of depth maps of a scene than methods which smooth the velocity field at motion boundaries. Clocksin (1980) showed that singularities in the Laplace transform of the flow field can be used to locate object edges. Together with information about surface slant, this information can be used to reconstruct the shapes of objects. Nakayama and Loomis (1974) proposed that a system of subtractive center-surround mechanisms operating on the velocity field could isolate the boundaries of an object independently of the observer's motion. In regularization methods for motion estimation it has become apparent that the fit to the true object motion is improved by introducing line processes across which smoothing does not occur (Shulman & Hervé, 1989; Murray & Buxton, 1987; Hutchinson, Koch, Luo & Mead, 1988; Black & Anandan, 1993).

Most psychophysical studies of motion perception have not been concerned with relative motion. The few that have considered relative motion have done so without explicit consideration for motion boundaries (Graham, Baker, Hecht & Lloyd, 1948; Nakayama & Tyler, 1981; Nakayama, Silverman, MacLeod & Mulligan, 1985; Nakayama, 1981; Golomb, Andersen, Nakayama, MacLeod & Wong, 1985; Snowden, 1992). In the most comprehensive set of studies on this issue, Nakayama and Tyler (1981) and Nakayama *et al.* (1985) measured sensitivity to motion of sinusoidal velocity fields consisting of random dots. Sensitivity was measured for different spatial frequencies of the velocity field, and a bandpass relationship was found: sensitivity was greatest for spatial frequencies around 0.4 c/deg, and decreased for higher and lower frequencies. This bandpass function suggests that local velocity responses across visual space are neither independent nor simply added together. Though sensitivity decreases for high frequencies measured in isolation, it is possible that high-frequency components could enhance sensitivity when they are combined to produce sharp motion boundaries. An explicit analysis of motion discontinu-

ities would therefore require additional measurements of sensitivity to combinations of frequency components.

There is, however, some empirical evidence that the visual system possesses special sensitivity for discontinuities in a velocity field. Zaidi and Sachtler (1992) measured direction-selective contrast thresholds for narrow strips of moving vertical gratings before and after adapting to moving gratings of the same orientation and spatial frequency as the test. In the first condition the adapting grating was 36 times the height of the test. The second condition was identical to the first except that the adapting grating was interrupted by a uniform bar within the test region, i.e. the test region was not exposed to the adapting grating but the motion boundaries at the edges of the test coincided with the motion boundaries of the adapting stimulus. Thresholds were elevated more following adaptation with the stimulus containing a uniform gap than with the stimulus which covered the test completely. Sachtler and Zaidi (1993) measured psychometric functions for motion of high-contrast sinusoidal gratings before and after adaptation to gratings moving in one direction. The adaptation effect was maximal when adapting and test gratings had the same dimensions, and decreased as the size of the adapting field was enlarged beyond that of the test. These results indicate that motion boundaries play a more important role in the detection of the test than the uniform velocity interior. Consistent with this interpretation are recent studies showing a greater sensitivity for shearing than for unidirectional motion (Sachtler & Zaidi, 1990; Snowden, 1992; Sachtler & Zaidi, 1994).

Experiments employing random-dot patterns have shown that vernier acuity is similar for motion-defined and luminance-defined stimuli that are normalized for sampling density and perceived contrast (Regan, 1986; Banton & Levi, 1993). Thus, if motion boundaries are extracted at some stage in the visual system, they may be used at a later stage to segment dynamic scenes with good spatial resolution.

These studies, however, did not provide direct evidence for, or against, processes that may be specialized to extract information at motion boundaries. In this study we compared sensitivity to different spatial forms of velocity gradients in an attempt to determine if motion boundaries are given special consideration in the visual system, i.e. whether sensitivity to motion is greater when stimuli contain sharp motion boundaries as opposed to more gradual spatial gradients of velocity. To do this, we compared sensitivity to horizontal shearing motion for various spatial velocity profiles made of independently moving lines of random dots, with the velocity of each line of dots being set by a vertical waveform.

In the first experiment we measured sensitivity for square-wave and sinusoidal velocity profiles at different phases and spatial frequencies. In the second experiment we used velocity fields created by spatial superposition of two sine waves. In the final experiment we created fluted velocity waveforms by subtracting the

fundamental sinusoidal component from square waves, retaining sharp motion boundaries between opposing directions but removing the regions of uniform motion. In the final section of this article we present a model that can account for the data by using linear center-surround velocity mechanisms whose sizes increase with eccentricity while their sensitivity for shearing motion decreases.

Equipment and stimulus generation

For all the experiments in this study, stimuli were presented on a 1280×1024 pixel 19 in. color monitor running at a rate of 60 frames/sec. The display was driven by a Silicon Graphics Personal Iris that permitted 8-bit specification of the intensity of each gun. To ensure linear control of the luminance generated on the screen the output of the three TV cathode guns was gamma-corrected by means of look-up tables. Mean luminance for all conditions was 34 cd/m^2 .

Stimuli consisted of random-dot fields presented within a 7.5×7.5 deg window surrounded by a 0.5 deg uniform border at mean luminance, as shown schematically in Fig. 1(a). The display window covered a region of 900×900 pixels. Since each random dot was allocated 10×10 pixels, there were 90 rows and columns of dots. Half of the 8100 available dots were randomly assigned to be light, the other half were kept dark. This produced a random field with no apparent structure, minimizing familiar position cues. Each line was begun at a random position outside the visible window so that dots would not fall within a strict rectangular array. Shearing motion was produced by moving horizontal lines of dots at different velocities, and a waveform was used to set the velocity on each line according to its vertical coordinate. In this way, different spatial velocity fields of horizontal motion could be produced. No compression took place since all dots on a line moved at the same velocity. Moving dots disappeared behind the edges of the stimulus window, i.e. the edges of the window were not warped.

Under the conditions of this study, measurements of motion threshold required that each stimulus element be moved less than 1 pixel per frame. Since motion appears jerky if stimulus elements are held stationary for several frames and then moved by 1 whole pixel, the method described below was used to generate continuous motion on each frame. Each dot was 7 pixels wide, and its edges had a slanted luminance profile as shown by the thick line in Fig. 1(b). This luminance profile was repeated for 10 lines of pixels in the vertical direction, so dots were 10 pixels tall \times 7 pixels wide, as indicated in Fig. 1(c). Pixels at the peak of the luminance profile were at maximum luminance (68 cd/m^2). High-contrast stimuli were used to avoid velocity-contrast tradeoffs (Thompson, 1982; Hawken, Gegenfurtner & Tang, 1994). In order to move a dot to the left, the luminances of the pixels on the left side were increased, while the luminances of the pixels on the right side were decreased by the corresponding amount, as shown by the small arrows in Fig. 1(b). A dot could be moved a fraction of

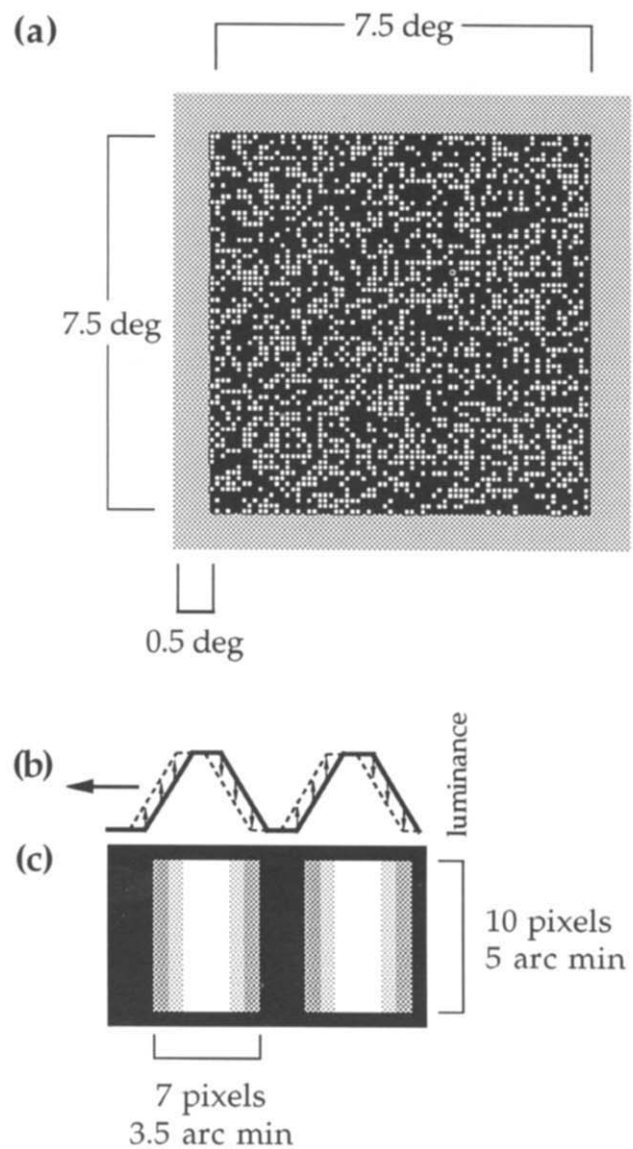


FIGURE 1. (a) Schematic of random-dot stimuli employed in this study. Half of the 8100 available dots were light, the others were dark. Each of the 90 horizontal lines of dots could move at an independent velocity, and each line was started at a random position so that dots did not fall within a strict rectangular array. The 0.5 deg wide surround was at mean luminance (34 cd/m^2). The stimuli were viewed in a dark room. (b) Luminance profiles of two adjacent dots as used in the random-dot display. Luminance is given on the vertical axis. The luminance distribution of a dot could be shifted by increasing the luminances of pixels on one edge while decreasing the luminances of the pixels on the other edge, as indicated by the small arrows. The resulting motion of the dots is indicated by the leftward arrow. A dot could be moved a fraction of a pixel by using a small luminance change. In order to give dots room to move, 3 pixels adjacent to each dot remained dark until they were lit up as needed to generate the luminance profile of the moving dot. (c) Frontal view of the dots whose luminance profiles are given above. The luminance profiles were repeated for 10 pixels in the vertical direction to generate dots with the dimensions shown. Motion was restricted to the horizontal direction.

a pixel by making a small luminance change. In order to give dots room to move, 3 pixels adjacent to a dot remained dark at the beginning of a trial so that adjacent dots were separated by a dark region, as shown in

Fig. 1(c). During a trial, these pixels were lit up as needed to generate the luminance profile of the moving dot. This method introduces a slight asymmetry into the luminance profile of the dot during motion, though the average luminance remains roughly constant and the asymmetry is not perceptible under the conditions used here. Each dot was restricted to a region 10 pixels square and could only move left or right.

The distance between the screen and the observer was kept constant at 181 cm by means of a fixed forehead and chin rest. At that distance, each pixel subtended 0.5 arc min, so that each dot was 5 arc min tall 3.5 arc min wide, as shown in Fig. 1(c). The screen was viewed binocularly, and artificial pupils were not used.

Observers

Two observers participated in the experiments. Observer WLS, one of the authors, was emmetropic, tested color normal on the Farnsworth–Munsell 100-hue test, and had extensive experience with psychophysical experiments. Observer AI, who was naive regarding the purpose of the experiments, was emmetropic, had previous experience with psychophysical experiments, and was given extensive practice to become acquainted with the psychophysical task employed in this study.

EXPERIMENT 1

In Expt 1 we measured sensitivity to motion of random-dot stimuli with sinusoidal or square-wave velocity fields for three spatial frequencies of the velocity waveforms, and for odd or even symmetric phases around the fixation point. These conditions allowed sensitivity to motion for stimuli with sharp motion boundaries to be compared to sensitivity to fields with more gradual spatial changes in velocity. Stimuli at different phases varied the eccentricity of the peak velocity and of motion boundaries, and provided information about differential sensitivity to these two types of motion information across retinal coordinates.

Stimuli

Four types of velocity waveforms were used in Expt 1: sine waves and square waves in odd and even phases around a central locus of fixation (Fig. 2). For illustration purposes, the amplitudes of the waveforms in the diagram are scaled according to the threshold values found experimentally, and will be described later. For the sine [Fig. 2(a)] and square [Fig. 2(b)] waves presented in odd phase, the zero-crossing was located at the fixation point in the center of the screen, which is indicated by a circle. As indicated by the arrows in the diagrams, dots above and below the fixation point moved in opposite directions. For the sine wave at f_1 , shown in Fig. 2(a), dots on the horizontal lines near the fixation point moved slowly, while dots further away moved the fastest, as indicated by the peaks of the sinusoidal curve. The velocities of the dots decreased again for lines nearer the edges of the stimulus window.

For the square wave at f_1 , shown in Fig. 2(b), all dots above the fixation point moved at one velocity, while all dots below the fixation point moved at the same speed but in the opposite direction. A motion boundary was defined at the fixation point by adjacent lines of dots moving in opposite directions. In the even phase presentations, the peak of the sine wave [Fig. 2(c)] or the middle of the uniform velocity region of the square wave [Fig. 2(d)], i.e. the highest velocity, was at the fixation point.

Three spatial frequencies of the velocity field were tested: 0.133, 0.4, and 1.2 c/deg. Exactly one cycle of a 0.133 c/deg waveform fit within the display window, and the higher frequencies were 3 and 9 times that frequency. These frequencies will be referred to as f_1 , f_3 , and f_9 throughout the paper. The waveforms for the different frequencies are shown schematically in the three rows in Fig. 2. Square waves are designated f_1 , f_3 , and f_9 according to the frequency of the fundamental harmonic.

Rightward motion was designated as positive velocity and leftward as negative. The amplitude of the velocity waveform was defined as one half the difference between

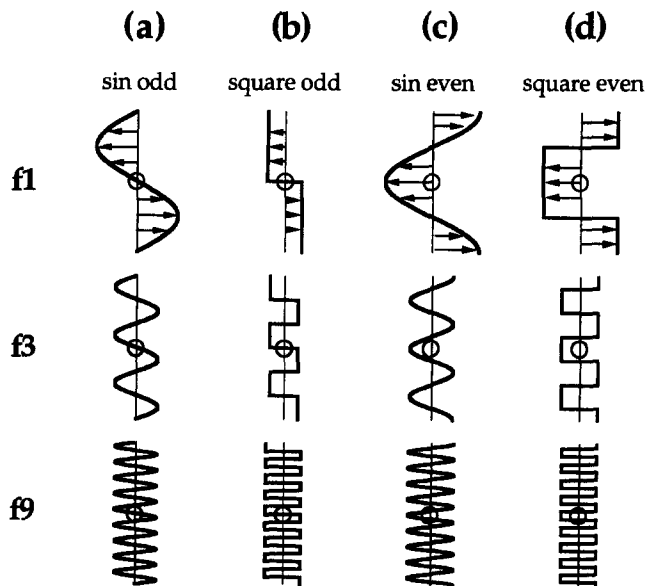


FIGURE 2. Spatial velocity waveforms used to set the velocity for each line of dots in the stimulus for Expt 1. The height of each profile corresponds to the vertical extent of the random-dot stimulus. The horizontal deviation of the solid curve from the center line corresponds to the velocity of the row of dots at a given location. Arrows indicate the direction of motion. The amplitude of a waveform was defined as half the difference between the peak and trough velocities. Sensitivity to motion was measured for different amplitudes of the waveforms. Waveforms in the diagram are scaled according to their amplitude at threshold (82% correct), as described in the text. Each waveform was tested at three spatial frequencies designated f_1 , f_3 , and f_9 , respectively, where the two highest frequencies were 3 and 9 times the fundamental. An integer number of cycles fit within the display window in each case. (a) Sinusoidal velocity fields in odd phase with respect to the fixation point (indicated by a circle). (b) Square-wave velocity fields in odd phase, i.e. the motion boundary between opposing directions of motion is at the fixation point. (c) Sinusoidal velocity fields in even phase. In this case, the peak velocity is at the fixation point. (d) Square-wave velocity fields in even phase. Peak velocity is at the fixation point.

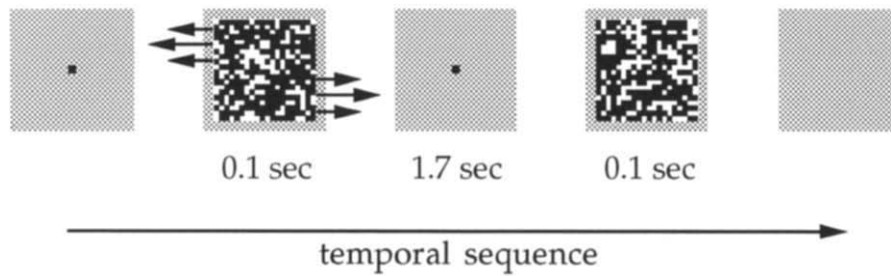


FIGURE 3. Temporal sequence from left to right of two-interval forced-choice procedure. Each trial began with a blank screen at mean luminance with a central fixation spot. The two test intervals were presented for 100 msec each separated by a 1.7 sec blank field. One test contained a field with a velocity profile, the other contained a stationary random-dot field. A different random-dot field was generated for each test presentation. The fixation dot was removed during the presentation of each test, and remained off after the second presentation until the observer made a response. The observer had to indicate which test interval contained the moving stimulus, and was instructed to guess when unsure.

the peak rightward and the peak leftward velocities. Since an integer number of cycles was used in all cases, the d.c. velocity component integrated across the screen was always zero.

Procedure

A two-interval forced-choice procedure, shown in Fig. 3, was used: in one test interval the dots moved at velocities determined by a vertical spatial velocity waveform as indicated by the arrows, while in the other the random-dot field was stationary. The order of stationary and moving stimuli was randomized on each trial. A trial began with a uniform screen at mean luminance, with a red fixation spot of 5 arc min diameter at the center of the screen. Three equally spaced tones cued the presentation of the test stimulus. The first test was presented for an interval of 100 msec at a constant velocity amplitude, which was equal to zero if it was the "stationary" interval. The screen was then immediately changed to a uniform field at mean luminance. After 1.7 sec the second 100 msec test interval was presented. A different random-dot field was generated for each test presentation. The fixation dot was removed during the presentation of each test, and remained off after the second presentation until the observer made a response. The observer had to indicate which test interval contained the moving stimulus, and was instructed to guess when unsure. A short tone sounded if the correct choice was made.

Psychometric curves for the detection of motion were measured for different velocity fields. Different amplitudes of the velocity waveform were presented for each condition, and the proportion of correct responses at each amplitude was recorded. Data for observer WLS were collected over eight sessions for a total of 80 presentations of each velocity for each stimulus. For observer AI, 50 trials were run over 10 sessions. In each session, data were collected for the two types of waveforms and their two phases at one spatial frequency. The four conditions and all velocity amplitudes tested were interleaved randomly. In addition, the sign of the waveform was varied at random, e.g. for sine odd at f_1 , the lobe above the fixation dot could move either left or right, with the direction of the other lobe in opposition

to that. Data were collected for a discrete set of velocities chosen by pilot runs to cover the complete psychometric range.

The test stimuli were presented for 100 msec because this is shorter than the time needed to initiate pursuit movements (Westheimer, 1954). The test stimulus moved throughout its presentation time, i.e. it was not stationary before and after the test motion. This is similar to opening and closing an aperture behind which a pattern moves at a constant velocity.

Results

Psychometric curves for the detection of motion for different velocity fields are shown in Fig. 4 for observer WLS and in Fig. 5 for observer AI. Each panel compares psychometric curves for the two waveforms shown schematically at the top of the column. Each psychometric curve is presented in two of the columns to allow different comparisons to be made. Each row in the figures shows all the psychometric curves at one spatial frequency, f_1 , f_3 , or f_9 , with the lowest frequency in the top row. Amplitudes of the velocity waveforms are indicated on the abscissa in deg/sec. Since all the waveforms were symmetric around zero velocity, the amplitude of each velocity waveform, $(\max - \min)/2$, is equal to the maximum absolute velocity present in the stimulus. The percentage of correct responses is shown on the ordinate. Chance performance is indicated by the dotted line at 50% correct in each panel.

The experimental results were fit with the following psychometric function (Quick, 1974; Watson, 1986):

$$P = 1 - \frac{1}{2} \exp \left[- \left(\frac{v}{\omega} \right)^\kappa \right], \quad (1)$$

where P is the probability of a correct choice, v is the velocity amplitude of the test stimulus, ω fixes the curve to a threshold velocity amplitude (at 82% correct), and κ controls the slope of the function.

A maximum-likelihood estimator was used to determine the best fit to each psychometric curve by assuming a binomial distribution of responses around the probability given by equation (1) (Hoel, Port & Stone, 1971; Watson, 1979). A Nelder-Mead (Nelder & Mead, 1965)

error-minimization routine was used to find the parameter settings giving the best fit to each psychometric curve. The curves fit the data well (χ^2 , $P < 0.05$). The only exception is for sine even at f1 for both observers, where the absence of a good fit seems to be due to noise in the data.

For each panel we tested whether the two psychometric functions of each comparison pair could belong to the same distribution. A single curve (not shown) was fit to the two sets simultaneously by the same procedure described above. The quality of the simultaneous fit was compared to the fit with two separate curves by transforming the likelihoods (L) obtained for these two conditions according to the following equation:

$$\lambda = -2 \ln \left(\frac{L(\text{data}|\text{single curve})}{L(\text{data}|\text{independent curves})} \right). \quad (2)$$

In this way, λ is distributed as χ^2 with two degrees of freedom (Hoel *et al.*, 1971). If λ exceeded the criterion value (for $P = 0.05$) we concluded that a single curve gave a significantly worse fit to the two data sets than two separate curves.

Results for the two observers were qualitatively similar, and statistical tests gave similar results in most

cases. Therefore, we discuss the results for observer WLS shown in Fig. 4; we address the results for observer AI only when they differ qualitatively from results for observer WLS.

In Fig. 4(a) we compare sensitivity to motion of square wave and sinusoidal velocity fields in odd phase, i.e. when the boundary between opposing directions was at the fixation point for both waveforms. Results for odd phase square waves are shown as solid squares, and results for odd phase sine waves as solid circles. At the lowest frequency, f1, the psychometric curve for the detection of motion for the square-wave velocity field is to the left of the curve for the sinusoidal velocity field. That is, sensitivity is greater for the stimulus with the sharp motion boundary. For frequencies f3 and f9 (bottom two panels), sensitivity for the sinusoidal velocity field is progressively greater, though it remains less than for the square wave. Separate curves for the two waveforms provided the best fit to the data at all frequencies.

In a separate analysis that is not illustrated in this figure we found that the psychometric curves for the square wave in odd phase for f1, f3, and f9 were very similar. Comparisons of f1 with f3 and f1 with f9 showed

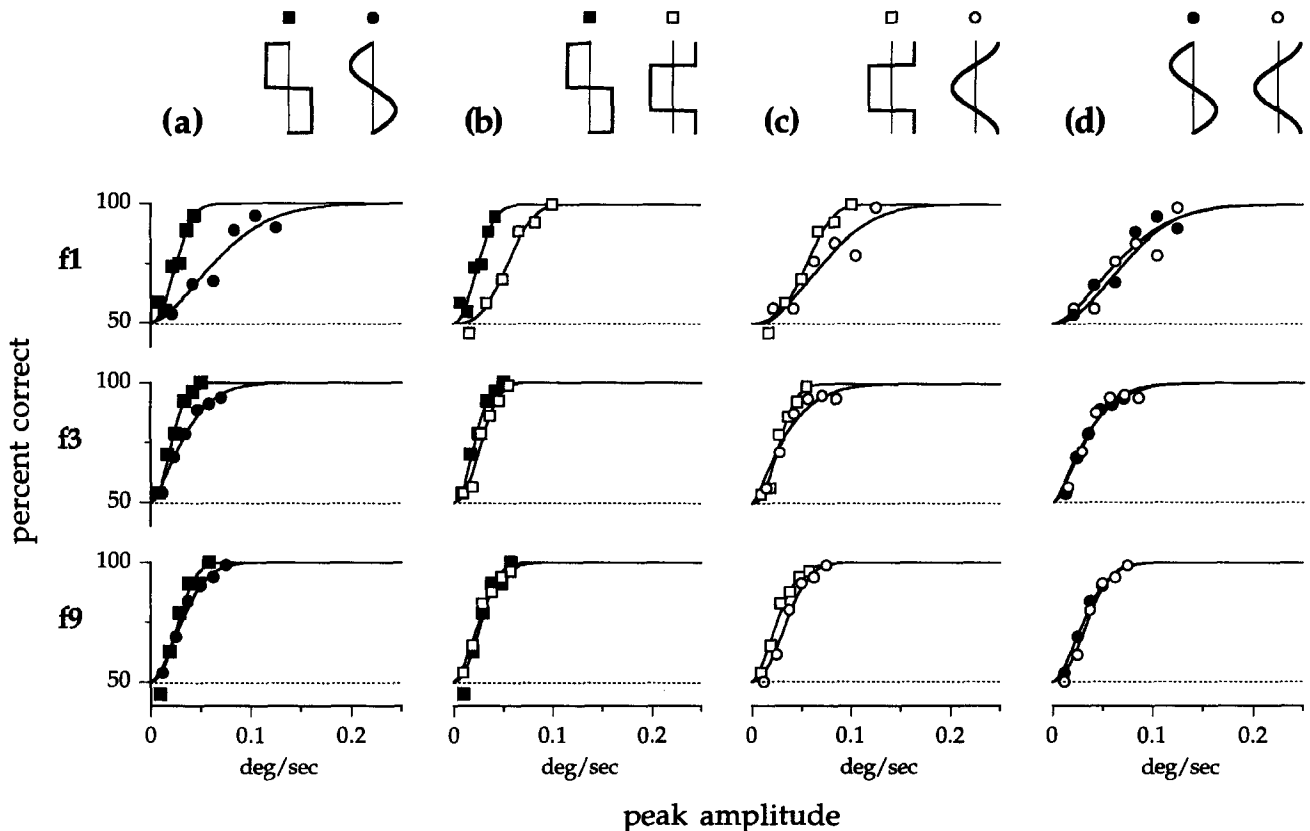


FIGURE 4. Results of Expt 1 for observer WLS: psychometric curves for the detection of motion for the velocity fields shown in Fig. 2. Each panel compares psychometric curves for the two velocity waveforms shown at the top of each column, with plot symbols as indicated above each waveform. Each set of results is repeated in one other panel for a different comparison. Each row of panels shows results at one spatial frequency, as indicated on the left (f1 = 0.133 c/deg, f3 = 0.4 c/deg, f9 = 1.2 c/deg). Amplitudes of the velocity waveforms are indicated on the abscissa in deg/sec. The percentage of correct responses is shown on the ordinate. Chance performance is indicated by the dotted line at the 50% level in each panel. For all experiments in this study, 80 trials were run for each data point for observer WLS. Solid curves show the best fitting psychometric functions from equation (1) to each data set.

that a single curve provided a satisfactory fit to each pair of results. Only the data for f3 and f9 was best fit with two separate curves.

Results for square wave velocity fields in odd and even phase are shown as solid and open squares, respectively, in Fig. 4(b). For f1, the psychometric curve for the even phase velocity field is to the right of the curve for the odd phase velocity field. Thus, for velocities around 0.04 deg/sec, motion is detected in approx. 90% of trials when the motion boundary is at the fixation point, while performance is only slightly above chance when it is not. For the even phase, the motion boundary was at 1.9 deg eccentricity. For higher frequencies there are additional motion boundaries in the stimulus and at least two of them are closer to the fixation point. As shown in the bottom two panels, sensitivity is greater at higher frequencies for the even phase stimuli, whereas for the odd-phase stimuli it is roughly constant. Data for the two waveforms were best fit with two separate curves at f1 and f3, while at f9 a single curve provided a satisfactory fit to the data.

In Fig. 4(c) we compare results for sinusoidal and square-wave fields in even phase, shown as open circles and squares, respectively. Both stimuli have their peak velocity at the fixation point. Sensitivity to square waves is slightly higher than for sine waves at all frequencies. The data sets for the two waveforms were best fit with two separate curves at all frequencies.

In Fig. 4 (d), results are shown as solid and open circles for sine-wave velocity fields in odd and even phase, respectively. In odd phase, the peak velocity is at 1.9 deg eccentricity, while in even phase it lies at the fixation point. Psychometric curves for the two conditions are similar to each other at each frequency tested for observer WLS (Fig. 4), and a single curve provided a satisfactory fit to the two data sets. For observer AI (Fig. 5), the psychometric curve for the sine even waveform lies to the right of the curve for the sine odd waveform and the data is best described with two separate fits.

Discussion

The results of Expt 1 show that sensitivity to motion is greater when the stimulus contains sharp motion boundaries than when changes in velocity across space are more gradual. An alternate explanation could be that one lobe of a square wave has a larger area than one lobe of a sine wave of the same amplitude, and that thresholds are proportional to the integrated area for motion. This hypothesis would imply that thresholds would be the same when the areas of the lobes are the same. The waveforms shown in Fig. 2 have been scaled according to threshold amplitude, i.e. the peak velocity at a value of 82% correct for observer WLS. At threshold, not only is the amplitude of the square wave smaller than of the sine wave, but so is the area of each lobe, thus refuting this hypothesis.

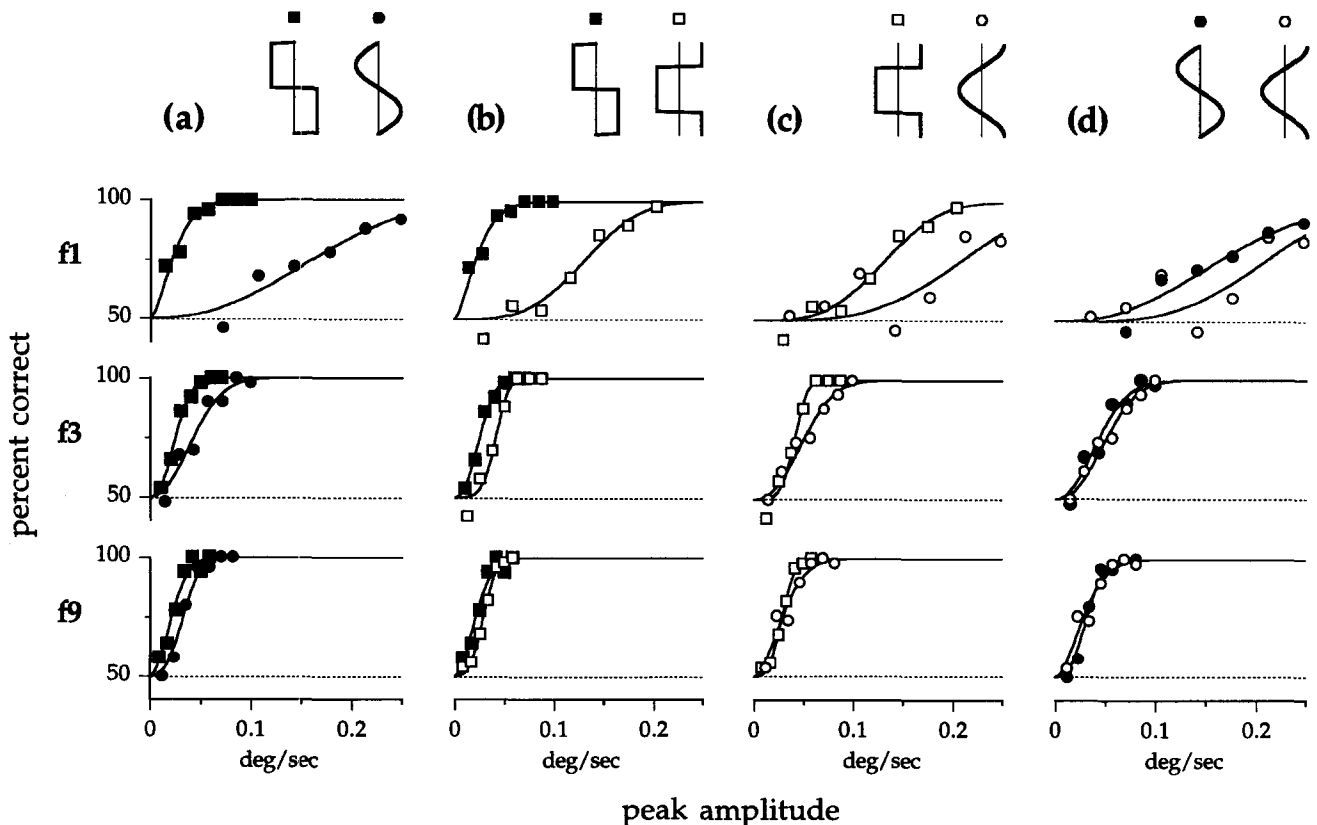


FIGURE 5. Results of Expt 1 for observer AI. All graphical conventions are identical to Fig. 4. For all experiments in this study, 50 trials were run for each data point for observer AI.

Another measure of the availability of motion information is the root-mean-square (r.m.s.) value of the velocity amplitude, calculated as the square root of the integral of the square of the waveform, divided by 2π (Lenert, 1970). Taking the 82% correct point from the best fit of equation (1) as the threshold velocity, the r.m.s. values for the square and sine waves at frequency f_1 are 0.012 and 0.022, respectively, for observer WLS, and 0.011 and 0.053 for observer AI. For both observers, the r.m.s. value at threshold is less for the square wave than for the sine wave, and thus cannot account for the greater sensitivity to motion when the square-wave velocity profile is presented. The possible effects of available integration area will be addressed further in Expt 3.

The processes underlying motion detection in this task cannot be characterized as a translation-invariant system because sensitivity to motion for the f_1 square waves in even and odd phases is greater when the motion boundary is at the fixation point than when it is at 1.9 deg eccentricity. The difference between the sensitivity for odd and even square waves is greater than the difference between the sensitivities for odd and even sine waves, indicating a greater inhomogeneity for the detection of sharp velocity discontinuities than for the detection of relatively shallow velocity gradients.

Nakayama *et al.* (1985), Nakayama and Tyler (1981) and Golomb *et al.* (1985) found a bandpass relationship for sensitivity to shearing motion with sinusoidal velocity fields of various frequencies: thresholds were lowest for spatial frequencies around 0.4 c/deg, and increased for frequencies higher and lower than that. Their task differed from ours in many aspects, including that stimuli were presented for a longer time interval and dots oscillated back and forth. Figure 6 shows velocity thresholds for sine waves and square waves in odd phase from Expt 1 for both of our observers. Thresholds for sine waves are shown as circles, and results for square waves as squares. Thresholds were chosen as the 82% point of the best fit of equation (1) to each psychometric curve. The lowest three frequencies shown correspond to f_1 , f_3 , and f_9 . The highest frequency data correspond to psychometric curves measured for an additional square wave velocity field at $f_{22.5}$ (3 c/deg), whose period length consisted of two lines of dots moving in one direction and two lines in the other direction. Sensitivity to square waves and sine waves at $f_{22.5}$ is expected to be similar, since the results of Expt 1 showed that sensitivity to sine waves increases with increasing spatial frequency and approaches that of square waves at f_9 . The functional form of our results is similar to that of Golomb *et al.* and Nakayama *et al.* in exhibiting the bandpass characteristic for sine waves. The minimum of these curves lies in the range of 0.4–1.2 c/deg, which is similar to the results found in other studies. The curves for the odd-symmetric square waves are low-pass and always below the sine wave curves. It seems that a sharp boundary at the fixation point leads to maximal sensitivity until the integration area is reduced drastically as for $f_{22.5}$.

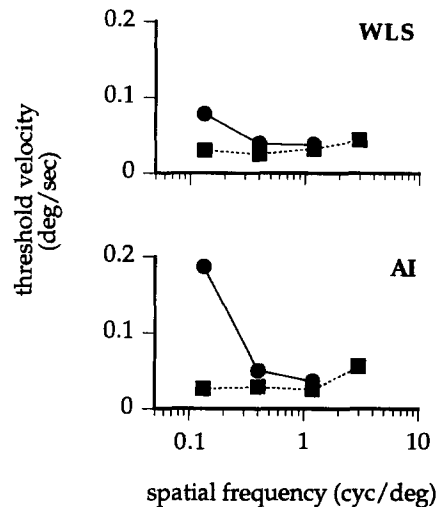


FIGURE 6. Velocity thresholds from Expt 1 for odd phase sinusoidal and square-wave velocity fields for both observers. Thresholds for sine waves are shown as circles, and results for square waves as squares. Thresholds were chosen as the 82% point of the best-fitting psychometric function for each data set taken from Figs 4 and 5. The lowest three frequencies correspond to f_1 , f_3 , and f_9 . Data for the highest frequency correspond to psychometric curves measured for an additional square-wave velocity field at 3 c/deg. Straight lines connect points of each data set for graphical purposes and have no theoretical significance.

EXPERIMENT 2

The results of Expt 1 indicated that the processes underlying detection of shearing motion cannot be characterized as a shift-invariant system. However, it is possible that the individual frequency components do determine sensitivity for stimuli with zero-crossings at the same retinal location. A square wave contains the odd-numbered higher harmonics in addition to the fundamental frequency. Since sensitivity to sine waves f_3 and f_9 was greater than for f_1 , sensitivity to motion may have been higher for the f_1 and f_3 square waves because of the presence of the higher frequencies. In this experiment we explore whether the presence of higher harmonics is sufficient to increase sensitivity for a compound stimulus, or whether increased sensitivity results from amplitude and phase combinations that generate sharp velocity gradients. In particular, we superimposed pairs of sinusoidal velocity fields in two different relative phases to produce either a steeper velocity gradient between opposing directions of motion or to produce a greater peak velocity. The empirical results were then compared with predictions from probability summation of the responses to the individual components.

Stimuli

In Expt 2, sine waves of two different frequencies were combined to form composite velocity waveforms. All sine waves were in odd phase, so that the zero-crossings were at the fixation spot. The same component frequencies were used as in Expt 1 ($f_1 = 0.133$ c/deg, $f_3 = 0.4$ c/deg, $f_9 = 1.2$ c/deg). Sine waves were com-

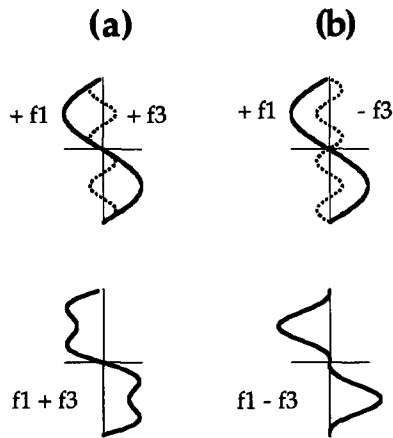


FIGURE 7. Velocity fields used in Expt 2. Sine waves of two different frequencies were superimposed to form composite velocity waveforms. All sine waves were in odd phase, so that the zero-crossings were at the fixation point. The same component frequencies as in Expt 1 were used ($f_1 = 0.133$ c/deg, $f_3 = 0.4$ c/deg, $f_9 = 1.2$ c/deg). Sine waves were combined by simple addition or subtraction of the components to yield four waveforms: $f_1 + f_3$, $f_3 + f_9$, $f_1 - f_3$, $f_3 - f_9$. The second member of a pair of frequencies was always the third harmonic of the first, and its amplitude was set equal to one-third of the amplitude of the fundamental. (a) Addition of the weighted components (top) leads to waveforms approximating square waves (bottom). (b) Subtraction of the weighted components (top) produces waveforms approximating triangular profiles (bottom).

bined by simple addition or subtraction of the components to yield four waveforms: $f_1 + f_3$, $f_3 + f_9$, $f_1 - f_3$, $f_3 - f_9$. The second member of a pair of frequencies was always the third harmonic of the first. The amplitude of the third harmonic was set equal to one-third of the amplitude of the corresponding fundamental. Addition of the weighted components, shown in the top panel of Fig. 7(a), leads to the waveforms approximating square waves shown in the bottom panel. Subtraction of the weighted components, top panel in Fig. 7(b), produces waveforms approximating triangular profiles shown in the bottom panel. The maximum velocity gradient in the waveform approximating a square wave is steeper than in the more triangular profile, whereas for the same amplitudes of the components, $f_1 - f_3$ has a peak velocity that is a factor of 1.4 higher than $f_1 + f_3$.*

Procedure

The same two-interval forced-choice procedure as in Expt 1 was used. Both types of waveforms at the two fundamental frequencies, f_1 and f_3 , and all test velocities were interleaved randomly within each test session. For observer WLS, data were collected over eight sessions

for a total of 80 presentations of each velocity. For observer AI, 50 trials spread over 10 sessions were run for each condition.

Results

Psychometric curves for the two combinations of sinusoidal velocity waveforms are shown in Fig. 8 for observer WLS and in Fig. 9 for observer AI. The top rows show results for combinations of frequencies f_1 and f_3 , while the bottom rows show results for combinations of f_3 and f_9 . Results for $f_1 + f_3$ and $f_3 + f_9$, which approximate a square wave, are shown as half-shaded squares, while results for $f_1 - f_3$ and $f_3 - f_9$, which have a more triangular profile, are shown as open triangles.

In Figs 8(a) and 9(a), results are plotted in terms of the peak amplitude of the combined waveform. For both waveforms, the velocity on the abscissa is equal to the maximum absolute velocity present in the stimulus. The best fitting psychometric functions from equation (1) for each data set are shown as solid lines. For the f_1 , f_3 combinations, sensitivity to motion is greater when the velocity field approximates a square wave than when it has a more triangular profile. For the f_3 , f_9 combinations, the psychometric curves for the two combinations are closer together, though squares still plot to the left of triangles. For both observers, each pair of data sets was best fit with two separate curves.

In Figs 8(b) and 9(b), the same data are re-plotted in terms of the amplitude of the fundamental frequency of the velocity waveform. Since the amplitude of the third harmonic was set as one-third of the amplitude of the fundamental, the amplitudes of both component frequencies are equated for the two conditions. The peak amplitudes of the combined waveforms differ by a factor of 1–4. When plotted on this scale, psychometric curves for the two conditions lie closer together for f_1 , f_3 in the top panel, and are superimposed for f_3 , f_9 in the bottom panel. In the top panel, squares lie to the left of triangles, indicating a greater sensitivity to the stimulus approximating a square wave than to the more triangular waveform. For both observers, the data were best described by two separate fits for the f_1 , f_3 combinations, while for the f_3 , f_9 combinations a single curve provided a satisfactory fit to the data. In Figs 8(c) and 9(c) the sensitivity to the two waveforms can be compared to the dashed lines showing the results predicted from probability summation of independent responses to the fundamental and the third harmonic. The independent responses to the component frequencies were estimated for each observer from the fits to the data for sine waves in odd phase for f_1 , f_3 , and f_9 shown in Figs 4 and 5. For the f_1 , f_3 combinations, the curve predicted from probability summation lies between the data sets, but its fit to each data set could be rejected (χ^2 , for $P = 0.05$). For the f_3 , f_9 combinations, the predictions from probability summation fit both data sets well for observer WLS. The curve for probability summation does not provide a good fit to the psychometric curve for $f_3 + f_9$ for observer AI, but does for $f_3 - f_9$.

*In the literature, the $f_1 + f_3$ condition, which involves the addition of two sine waves of the same phase, is sometimes called the "peaks subtract" condition. Similarly, the $f_1 - f_3$ condition, where a sine wave is subtracted from another sine wave of the same phase, is sometimes called the "peaks add" condition.

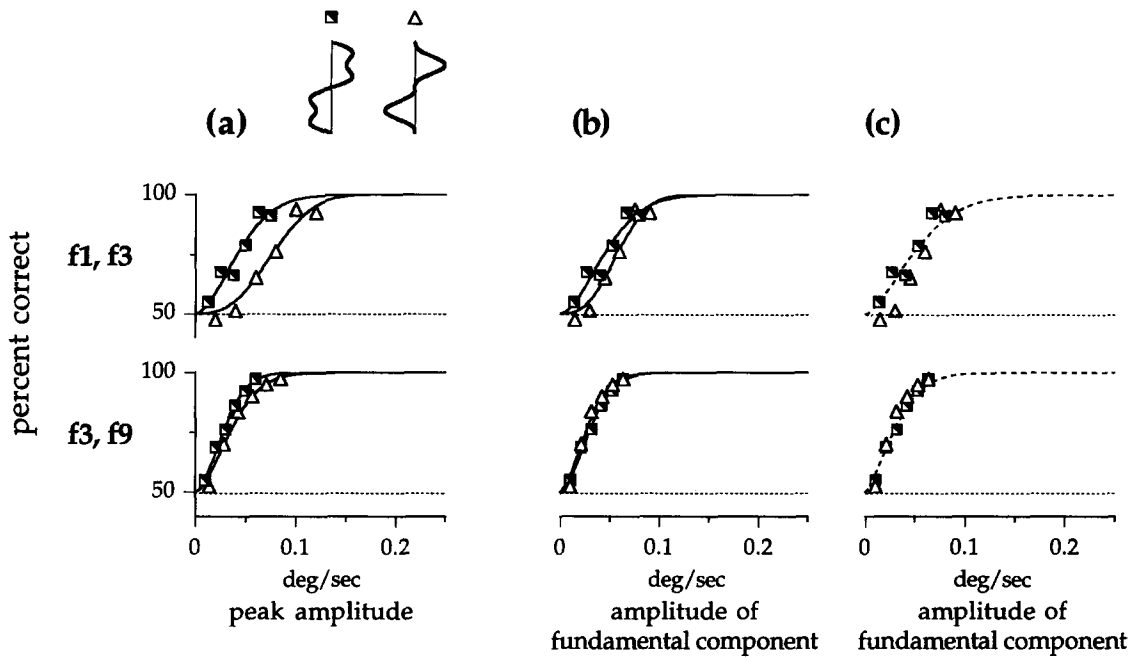


FIGURE 8. Results of Expt 2 for observer WLS. Each panel shows psychometric curves for the detection of motion for sums of sinusoidal velocity components approximating a square wave (squares), and for differences of components with a more triangular profile (triangles). The waveforms are shown above the plots. Results for combinations of f_1 and f_3 are shown in the top row, and those for f_3 and f_9 in the bottom row. (a) percent correct plotted against the peak amplitude of each composite waveform shown at the top. Solid curves show the best fitting psychometric function from equation (1) to each data set. (b) The same data as in (a) re-plotted in terms of the amplitude of the fundamental frequency of each velocity waveform. Since the third harmonic is always at one-third of the amplitude of the fundamental, the amplitudes of both component frequencies are equated for the two compound stimuli on the abscissa. Solid curves show the best-fitting psychometric function from equation (1) to each data set. (c) Same data and axes as in (b). The dashed lines show the results expected from probability summation of independent responses to the two component frequencies, estimated from the fits to the data for individual sine waves in odd phase (Expt 1).

Discussion

The results of Expt 2 show that sensitivity to compound shearing velocity fields depends on the relative phase of the components, and cannot be explained by independent detection of the components. Sensitivity was greater for the phase combination with the steeper velocity gradient and smaller peak amplitude even when the amplitudes of the sinusoidal components were equated for the two compound waveforms. The results therefore support the interpretation that the mechanisms underlying detection of motion are particularly sensitive to steep velocity gradients.

EXPERIMENT 3

In Expts 1 and 2 observers showed greater sensitivity to the "squarer" velocity profiles. Besides sharper velocity gradients, these profiles also possessed larger areas of uniform velocity. Even though our analysis of Expt 1 showed that at threshold the total integrated motion in each lobe of the f_1 square waves was less than the integrated motion in the f_1 sine waves, in Expt 3 we directly compared the importance of motion boundaries in motion detection to that of extended regions of uniform velocity.

Stimuli

Fluted velocity waveforms were generated by subtracting the fundamental sinusoidal component from a square wave in odd phase, as shown in Fig. 10(a). The resulting stimulus retains the sharp motion boundary and the peak amplitude of the square wave, while the area of uniform motion in each lobe is greatly reduced, as shown in Fig. 10(b). Flutes were generated for square waves with the fundamental frequencies f_1 , f_3 , and f_9 equal to 0.133, 0.4, and 1.2 c/deg. All stimuli were in odd phase, so that a motion boundary was located at the fixation point. Since the amplitude of the fundamental harmonic is 1.27 times that of the square wave, subtracting the fundamental component produces a small undershoot in the waveform within each lobe.

Procedure

We used the same two-interval forced-choice procedure as in Expt 1. All three frequencies of the fluted waveform and all test velocities, were interleaved randomly within one test session. For observer WLS, data were collected over eight sessions for a total of 80 presentations of each velocity. For observer AI, 50 trials spread over 10 sessions were run for each condition.

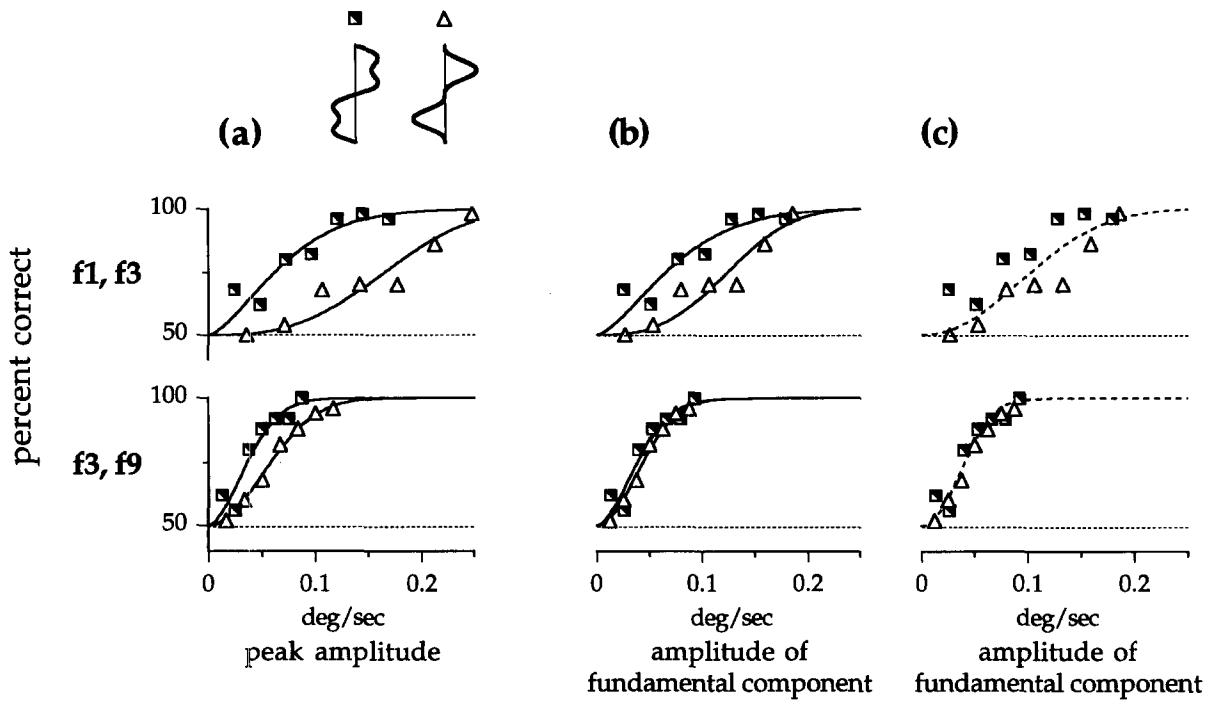


FIGURE 9. Results of Expt 2 for observer AI. All graphical conventions are identical to Fig. 8.

Results

Psychometric curves for the detection of motion for the three fluted velocity profiles are shown together with results for the corresponding square waves in Figs 11 and 12 for observers WLS and AI, respectively. Results for fluted waveforms are shown as open diamonds, results for square waves as solid squares. The best fitting psychometric functions from equation (1) are shown as solid lines through each data set.

In the top panel in Fig. 11, the psychometric curve for flutes is slightly to the left of the curve for square waves. That is, sensitivity to motion is slightly greater with the fluted waveform than with the corresponding square wave at f1 for observer WLS. A fit with a single curve

was significantly worse than with two separate curves. For observer AI, as shown in Fig. 12, psychometric curves are similar for flutes and square waves. One curve fit the two data sets as well as two separate curves. For f3 and f9, open diamonds plot to the right of solid squares. That is, sensitivity to motion was lower for flutes than for the corresponding square waves. This was true for both observers. In addition, sensitivity for flutes at f9 was lower than at f3 for both observers.

Discussion

The result that at f1 sensitivity to motion was no lower for flutes than for square waves indicates that for an extended stimulus large areas of uniform motion are not as important as sharp motion boundaries in detecting motion. Since the flutes differ from square waves only in the exclusion of the fundamental harmonic, the sensitivity to f1 flutes can be explained by the presence of higher harmonics combined in a manner to produce the sharp motion boundary. If local motion signals need to be sampled over some minimum area, the loss of sensitivity for flutes at f3 and f9 and to square waves at f27 could be because the largest integration area available from these stimuli is less than the minimum required for motion.

SUMMARY OF EXPERIMENTAL RESULTS

We have studied the role of motion boundaries in the detection of motion. Taken together, the results show that sensitivity to motion is greatest when there is a sharp velocity discontinuity at the fixation point. For motion detection, given the presence of a central motion boundary, the velocity profile of the rest of the stimulus

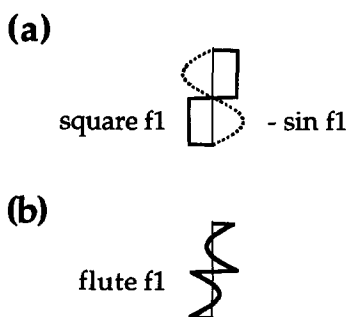


FIGURE 10. Velocity fields used in Expt 3. (a) The fundamental sinusoidal component is subtracted from a square wave in odd phase. The higher harmonic components remain unchanged. (b) The resulting fluted waveform retains the sharp motion boundaries between opposing directions of motion but lacks extended areas of uniform motion. Flutes were generated from square waves with fundamental frequencies f1, f3, and f9.

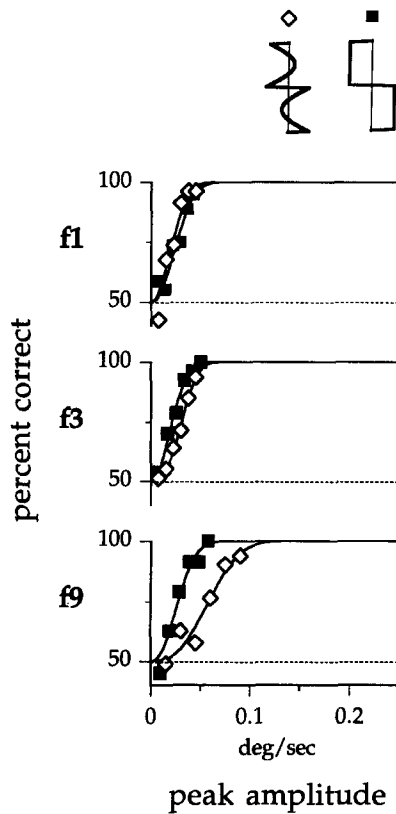


FIGURE 11. Results of Expt 3 for observer WLS. Panels show psychometric curves for the detection of motion of fluted velocity profiles (open diamonds). For comparison, results for square waves in odd phase are shown as solid squares. Each panel shows results for waveforms of one fundamental spatial frequency: Solid curves show the best fitting psychometric function (Eqn. 1) for each data set. Peak velocity amplitude of each waveform is given on the abscissa. The ordinate shows the percentage of correct choices of the interval with the motion signal. The horizontal dotted line in each panel shows 50%, or chance, performance.

is essentially irrelevant as long as there is a minimal integration area for velocity on either side of the boundary. As the phase of a compound velocity profile is changed, sensitivity is a function of the eccentricity of the most central motion boundaries. When sinusoidal velocity profiles are combined to generate sharp velocity gradients, sensitivity is greater than would be predicted from probability summation of responses to individual components.

It is important to list the set of conditions that the results of the present experiments may be limited to. First, these experiments were restricted to fairly low velocities at which motion could barely be detected. The processing of motion boundaries at higher velocities remains to be explored. Second, in these stimuli, all velocity components were parallel to each other and uniform along each horizontal line. Under conditions that involve transparent motion, where velocity components in different directions may overlap within a region, it has been reported that there is a greater sensitivity for shearing than for uniform motion, but no special role for motion boundaries (Watson & Eckert, 1994). Under conditions of transparent motion, motion

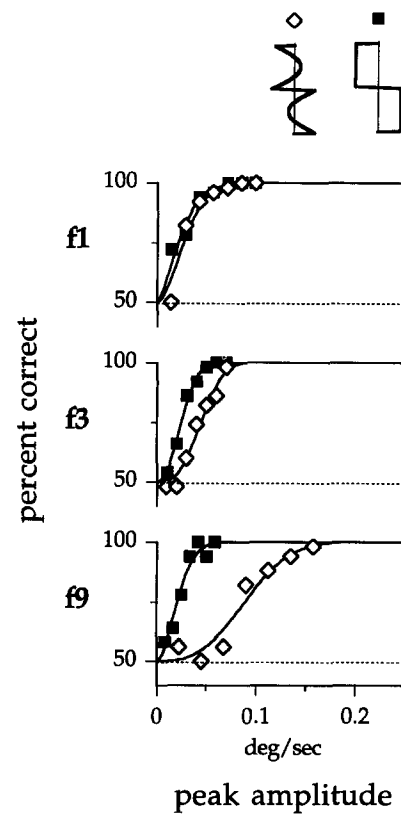


FIGURE 12. Results of Expt 3 for observer AI. All graphical conventions are identical to Fig. 11.

boundaries may not be as useful in segregating areas of uniform motion. Addition of noise may also disrupt detection of motion boundaries. For example, van Doorn and Koenderink (1982, 1983) found that the percept of a motion boundary disappeared with the addition of random noise before the percept of coherent motion. Since observers can identify the direction of coherent motion when random motion is added to coherent motion in random-dot fields (Watamaniuk, Sekuler & Williams, 1989), this class of stimuli may require the observer to extract the mean direction of the random dots while ignoring the presence of local sharp velocity gradients in random directions. The addition of random noise or transparency to the stimulus may thus change the nature of the observer's task from our conditions.

The results of the experiments in this study suggest that motion boundaries may in fact play an important role in the processing of motion information. An enhanced representation of motion boundaries would be useful in segregating moving objects from one another and the background, and helping to establish a depth layering of objects. The empirical results place constraints on mechanistic models of motion detection.

MECHANISTIC MODEL FOR THE PROCESSING OF SHEARING MOTION

In this section we present a model that can account for the experimental results of this study. This

model is based on mechanisms whose surround response to motion is subtracted from the center's response to motion in the same direction. We used an array of such units to generate probabilities of correct responses to the different velocity profiles used in the experiments.

Opposed center-surround motion mechanisms were previously suggested but not fit to experimental data (Nakayama & Loomis, 1974; Nakayama & Tyler, 1981; Clocksin, 1980; Koenderink & van Doorn, 1992). By analogy to the processing of luminance contrast by center-surround units (Ratliff, 1965), motion center-surround units will respond well to a shearing stimulus. It is far from clear, though, whether such a model is sufficient to account for the variety of results presented in this study.

In this section we will begin by giving a detailed description of the model, followed by a discussion of its performance in explaining the experimental results. This model is only one way to implement the principles necessary to capture the properties of the data, and we will discuss these principles in the context of the model. Subsequently, we will describe other ways to implement models with similar properties. For this, we discuss parameters that we left out for simplicity but which

could be added as plausible properties of a spatial sampling system. In addition, we discuss the elements necessary to successfully implement a model in which the receptive field shape consists of adjacent opposed lobes. Finally, we discuss some plausible receptive fields and computational approaches that do not give satisfactory results.

Description of model

In the model we assume that the velocity at each point in the stimulus is sampled by elementary motion-sensing mechanisms, shown as a column of gray ovals on the left of Fig. 13(a). These units are all maximally sensitive to motion along the horizontal, giving signed responses to motion in the two directions along that axis, and can be similar to any of a number of spatio-temporal energy mechanisms, e.g. Adelson and Bergen (1985). For simplicity we assume that the image is sampled by mechanisms whose output corresponds to the velocity at that point in the image. Even though the responses of model motion-sensing mechanisms are generally not linear over large velocity ranges, and often are non-monotonic, they can be considered approximately linear within the small velocity range near motion thresholds.

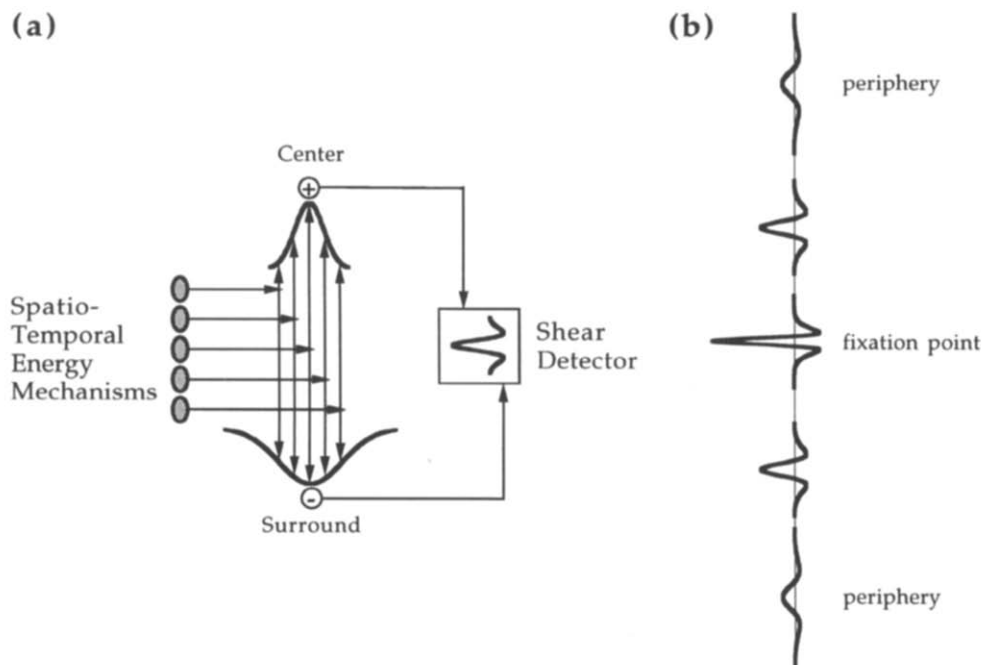


FIGURE 13. (a) Schematic of model incorporating linear shear-sensing mechanisms used to explain the experimental results. The velocity on each line of dots in the stimulus is sampled with elementary motion-sensing mechanisms tuned to motion in the horizontal direction, shown as gray ellipses on the left. The stimulus is sampled with a column of 110 such non-overlapping motion-sensing mechanisms: 90 for the moving display (one for each line of dots), and 10 above and below the display window. The responses of motion-sensing mechanisms are then fed into a network which sums the weighted responses of nearby mechanisms, as indicated by the rightward arrows. The heights of the Gaussian curves labeled "Center" and "Surround" indicate the weight assigned to each response. The center unit sums responses over a smaller region than the surround unit. The summed values of the center-surround subunits are then subtracted from each other, and constitute the response of the difference of Gaussians, or shear-sensing mechanism, shown on the right. One pair of center and surround subunits is centered over each elementary motion-sensing mechanism. (b) Sizes of shear-sensing mechanisms vary with eccentricity. Units near the central fixation point are smaller, while units further in the periphery are larger. Sizes of the center and surround subunits are scaled independently of one another. Responses of all shear-sensing mechanisms to a stimulus are combined through probability summation to generate probability of correct response.

At the next stage, in Fig. 13(a), the outputs of the local motion sensors are combined linearly through spatial weighting functions into shear sensors by feeding the responses into two summation units, labeled Center and Surround. The height of the Gaussian curves represents the weight assigned to the output of each elementary motion-sensing mechanism. The summed values of the Center and Surround subunits are then subtracted from each other, and constitute the response of the difference of Gaussians shown on the right.

Responses are summed linearly within each Gaussian, as described in equations (3) and (4):

$$C_j = \sum_{i=1}^{110} \left\{ v(i) \left[\frac{1}{\sigma_c W_c(j) \sqrt{2\pi}} \times \exp\left(-\frac{1}{2} \left\{ \frac{i-j}{12\sigma_c W_c(j)} \right\}^2\right) \right] \right\}, \quad (3)$$

$$S_j = \sum_{i=1}^{110} \left\{ v(i) \left[\frac{1}{\sigma_s W_s(j) \sqrt{2\pi}} \times \exp\left(-\frac{1}{2} \left\{ \frac{i-j}{12\sigma_s W_s(j)} \right\}^2\right) \right] \right\}. \quad (4)$$

C and S designate the Gaussians that constitute the center and the surround, respectively with standard deviations σ_c and σ_s in degrees of visual angle. Both

Gaussians have unit area and $\sigma_c < \sigma_s$. The parameter j designates the unit at which a Gaussian is centered. The velocity response $v(i)$ at any point i is weighted by the Gaussian centered at j . The index i ranges over the 110 sampling points described below, and the constant 12 is used to convert number of points spanned by the Gaussian to degrees of visual angle. The values of W_c and W_s in equations (3) and (4) modify the widths of the Gaussians as a function of distance from the fixation point. The values of W_c and W_s are calculated using the following equations:

$$W_c(j) = \begin{cases} 1 + m_c(55 - j) & \text{for } 1 \leq j \leq 55 \\ 1 + m_c(j - 56) & \text{for } 56 \leq j \leq 110 \end{cases}, \quad (5)$$

$$W_s(j) = \begin{cases} 1 + m_s(55 - j) & \text{for } 1 \leq j \leq 55 \\ 1 + m_s(j - 56) & \text{for } 56 \leq j \leq 110 \end{cases}. \quad (6)$$

W_c and W_s are equal to 1.0 for the two points in the center of the visual field and increase linearly towards the periphery with independent m_c and m_s . Thus, center and surround sizes were scaled independently of each other.

The final stage of the shear-sensing mechanism in Fig. 13(a) consists of the difference of the summed center and surround responses:

$$DOG_j = C_j - S_j. \quad (7)$$

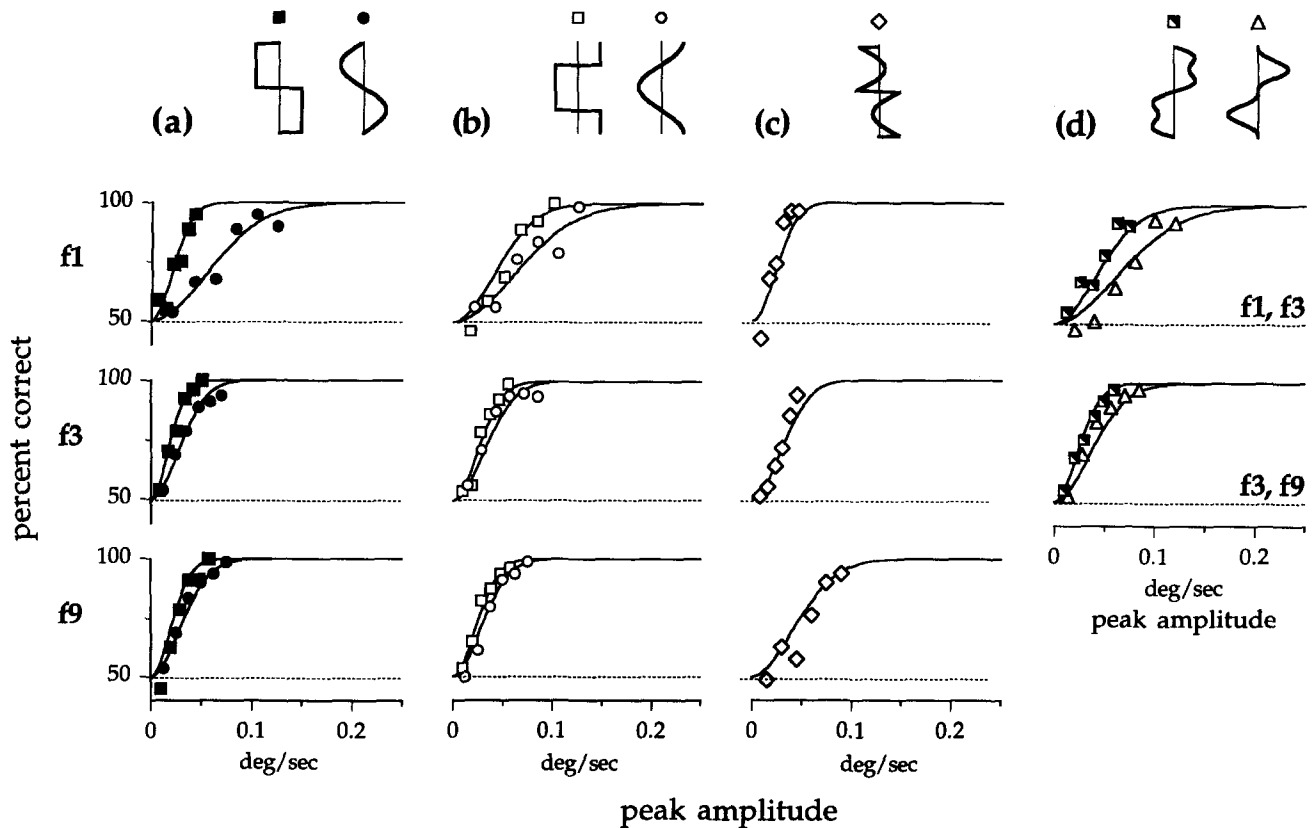


FIGURE 14. Psychometric curves generated by the model (solid lines) and results of Expts 1, 2, and 3 for observer WLS. The six parameters of the model were optimized to simultaneously fit all psychometric curves ($\sigma_c = 0.039$, $\sigma_s = 0.324$, $m_c = 0.984$, $m_s = 0.118$, $\alpha = 1.898$, $\beta = 0.0545$). (a, b) Results of Expt 1 for sine and square waves in odd and even phase. (c) Results of Expt 3 for fluted waveforms. (d) Results of Expt 2 for sums and differences of two sinusoidal components.

The schematic on the right of Fig. 13(b) shows how the sizes of shear-sensing mechanisms vary with eccentricity. Difference of Gaussians units are narrowest at the central fixation point, while peripheral units are broader.

In this model we sampled the stimulus along only one vertical axis, since all the dots in a horizontal line in our stimuli moved at the same velocity. This reduction in the sampling space loses information about the responses of mechanisms tuned to motion in other directions, but since the greatest velocities are along the horizontal direction, thresholds are mainly determined by these components. This simplification was justified by the good fits to the data. The model can easily be expanded into two-dimensional shear detectors.

The stimulus was sampled at 90 discrete points, which corresponded to the number of lines of dots in the experimental stimulus. In order to allow for responses of shear sensors whose centers lie outside the region of the stimulus, an additional 10 points were sampled above and below the edge of the stimulus, for a total of 110 points. Since dots could only move along the horizontal, velocities were designated negative for leftward motion and positive for rightward velocities. Velocity profiles were generated the same way as in the experiments, with a spatial waveform determining the velocity on each line of the stimulus. Velocity profiles

were restricted to the central 90 sampling points in the model, with the surrounding 20 points being assigned values of zero.

A shear sensor was centered at each of the 110 points sampled in the image. The responses of all 110 shear sensors were combined probabilistically using the Quick (1974) psychometric function:

$$P_{\text{detect}} = 1 - \prod_{j=1}^{110} [1 - (1 - 2^{-(\text{DOG}_j/\beta)^\alpha})]. \quad (8)$$

P_{detect} is the probability of detecting motion, the parameter β determines the response at which detection equals 50% for a single shear sensor while α is used to vary the slope of the psychometric curve. The probability of being correct in a two-interval forced-choice procedure needs to incorporate those trials in which motion was not detected but a correct response was given by chance:

$$P_{\text{correct}} = P_{\text{detect}} + (1 - P_{\text{detect}})/2. \quad (9)$$

In this form, the model has six free parameters: σ_c and σ_s , the standard deviations of the center and surround Gaussians, m_c and m_s , the slopes of the increase in size with eccentricity of the center and surround, and α and β for the function generating probability of detection. A Nelder-Mead (Nelder & Mead, 1965) error-minimization routine was used to find the parameter

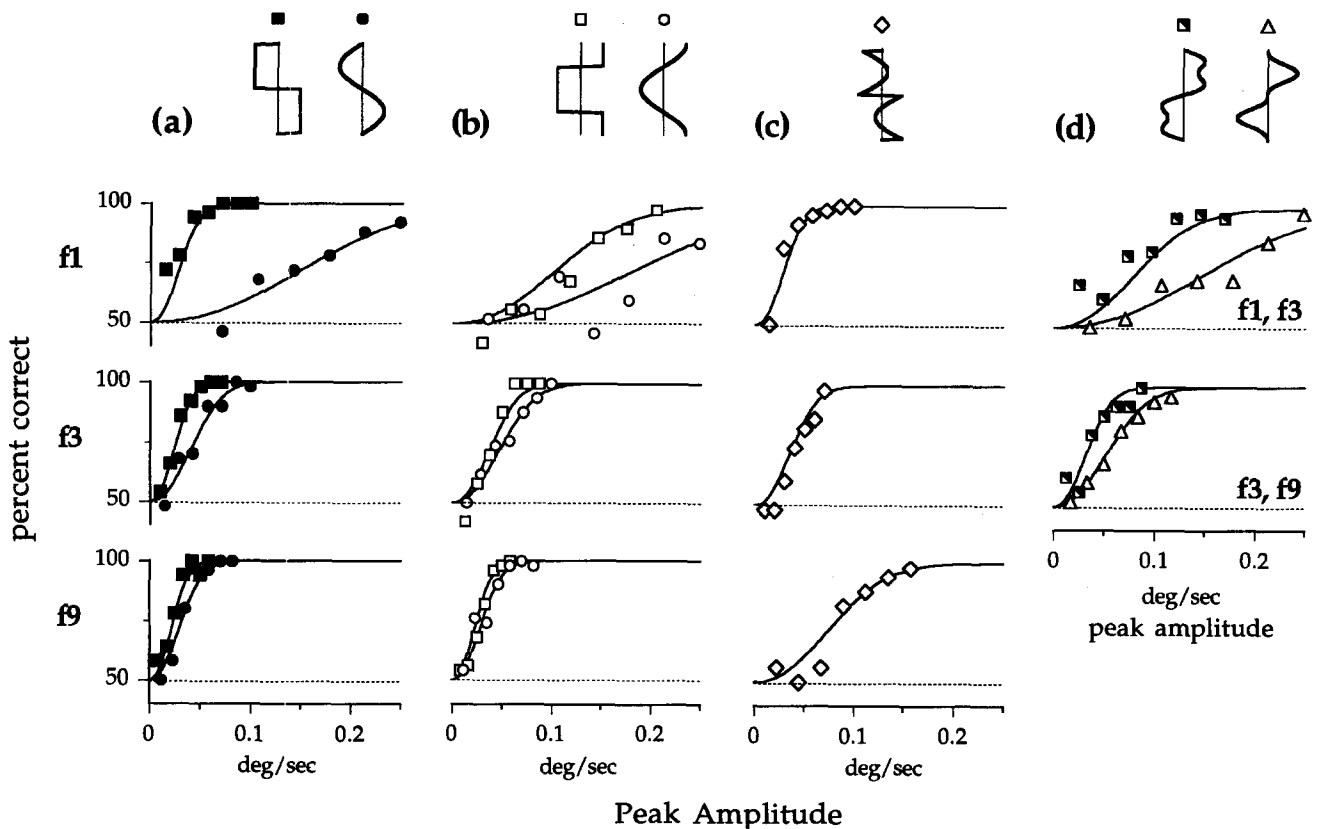


FIGURE 15. Psychometric curves generated by the model (solid lines) and results of Expts 1, 2, and 3 for observer AI. Parameter settings for optimal fit: $\sigma_c = 0.06$, $\sigma_s = 0.273$, $m_c = 0.653$, $m_s = 0.123$, $\alpha = 2.219$, $\beta = 0.0368$. All graphical conventions are identical to Fig. 14.

settings giving the best simultaneous fit of the model's probabilities of detection to all data sets for each observer. In this way, six parameters were used to fit 19 psychometric curves containing a total of 114 data points for observer WLS and 133 data points for observer AI.

Modeling results

Probabilities of detection generated by the model and the corresponding experimental results are shown in Figs 14 and 15 for observers WLS and AI, respectively. The model's parameter settings were different for each observer, and are given in the figure captions.

It is apparent that the model's predictions fit the complete data sets for both observers almost as well as the psychometric functions fit previously to each curve separately. The results of Expt 1 on sensitivity to square-wave and sinusoidal velocity fields are shown in Figs 14(a, b) and 15(a, b). In columns (a), the model accounts for the greater sensitivity to square waves than to sine waves in odd phase. In addition, the increase in sensitivity to sine waves at increasing frequencies is also accounted for. In columns (b), the model exhibits the decreased sensitivity for square-wave stimuli in even phase. Furthermore, sensitivity for square waves in even phase increases for higher frequencies. For observer AI, the model psychometric curve for square waves in even phase at f1 is somewhat shallower than the experimental results, shown as open squares. The model also captures the greater sensitivity to square waves than to sine waves when both are in even phase. Finally, the model's responses to sine waves in odd and even phase are very similar, reflecting the experimental results.

Results for Expt 2 on combinations of sinusoidal waveforms are shown in Figs 14(d) and 15(d). The model exhibits the greater sensitivity to the compound stimulus with the steeper velocity gradient for both frequency combinations tested and for both observers. The model's predictions for f1 + f3, shown as lines fit to the squares in the top panels, are somewhat to the right of the experimental results, indicating that the model is less sensitive to the stimulus with the steeper velocity gradient than observed empirically. For observer WLS, the model exaggerated the difference between f1 - f3 and f3 - f9 by generating a lesser sensitivity to the stimulus with the shallower velocity gradient than expected from the experimental results.

Figures 14(c) and 15(c) show results for fluted waveforms from Expt 3. For observer AI, the fits are quite good, and show that the lack of an area of uniform motion in flutes at f1 does not affect sensitivity to motion. The model generates a somewhat greater sensitivity for the flute at f3 than the empirical results. Model fits are also good for observer WLS, but point out a limitation of the model: the empirical psychometric curves for flutes f1 are steeper than the curves for the corresponding square waves. The curves generated by the model could fit the square-wave data, but are somewhat shallower than the experimental results for flutes. Square-wave and fluted waveforms employed in

these experiments have similar motion boundaries, but differed in the strength of the motion signal in the nearby regions. The response of a linear receptive field, which simply sums responses within a region, will be smaller at the motion boundary of the flute than of the square wave simply because the available motion signal is smaller over the area covered by the receptive field. Thus, the response to the fluted waveform cannot be greater than to the corresponding square wave. The difference between the responses at the motion boundaries of the two waveforms can be reduced by making the receptive field small, so that the difference in motion signal over the integrated area is minimized.

The key properties of the model that explain differences in sensitivity between different waveforms are captured by the center-surround antagonism and the independent scaling of center and surround receptive field sizes. The center-surround antagonism establishes the preference for shearing motion, as well as the bandpass characteristics for sinusoidal velocity fields. For very low frequencies of the waveforms, the responses of the center and the surround fields will tend to be similar, and thus will tend to cancel out. For very high frequencies, leftward and rightward components will tend to cancel out within each region, while for intermediate frequencies responses can differ greatly between center and surround, leading to maximal responsivity.

Scaling the receptive field sizes with eccentricity makes the system sensitive to the phase of the compound velocity waveforms for two reasons. First, the frequency characteristics change with eccentricity. Second, by scaling the center and surround independently, sensitivity to shearing motion can be reduced as a steep function of eccentricity. Figure 16(a, b) shows the sizes of the center and surround subunits at each eccentricity for the two observers as a function of distance from the fixation point, where the edge of the stimulus corresponds to 3.75 deg. Sizes are plotted as solid lines for center subunits and as dashed lines for surround subunits. The ordinate gives the size of each subunit in terms of the standard deviation of the pooling Gaussian in degrees of visual angle. At the fixation point, $\sigma_c = 0.039$ deg and $\sigma_s = 0.324$ deg for observer WLS; and $\sigma_c = 0.06$ deg and $\sigma_s = 0.273$ deg for observer AI. Parameters for observer AI in Fig. 16(b) show most clearly how the loss of sensitivity is achieved in the model: the sizes of center and surround become more similar towards the periphery until they become identical. Since the response of a shear sensor depends on the difference in responses between center and surround subunits, the difference is always zero when center and surround are the same size and area, no matter what the input.

Figure 16(c) elaborates this property of the model by showing the ratio of the sizes of surround to sizes of center units as a function of retinal eccentricity. A value of 1.0 indicates that both subunits are the same size and therefore that the shear sensor is insensitive to moving stimuli. Large values of the ratio indicate that the center and surround subunits differ greatly in size, and

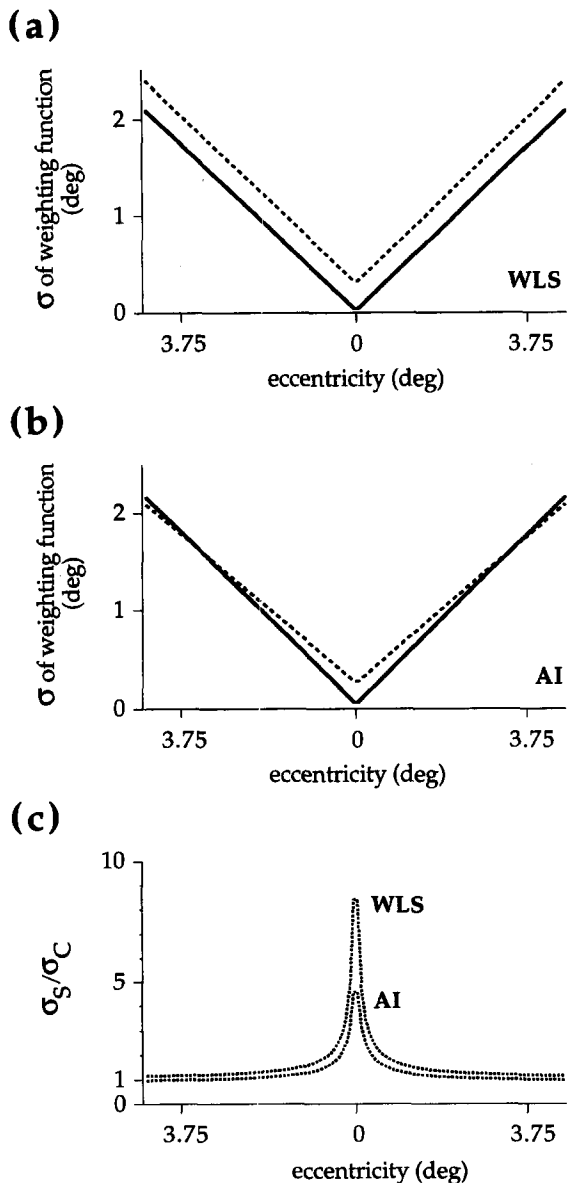


FIGURE 16. (a) Sizes of center and surround subunits at different eccentricities for parameter settings generating model fits shown in Fig. 14 for observer WLS. Solid and dotted lines show sizes of center and surround subunits, respectively, as a function of distance (in degrees of visual angle) from the fixation point. The edge of the stimulus corresponds to 3.75 deg. The ordinate gives the SD of each subunit in degrees. At the fixation point, $\sigma_c = 0.039$ deg and $\sigma_s = 0.324$ deg. 1 deg corresponds to 12 elementary motion-sensing units. (b) Sizes of center and surround subunits for model fits shown in Fig. 15 for observer AI. At the fixation point, $\sigma_c = 0.06$ deg and $\sigma_s = 0.273$ deg. (c) Ratio of size of surround to size of center subunits taken from (a) and (b) for both observers.

therefore respond well to shearing motion. The plot shows that ratios are greatest at the center of the model's visual field for both observers and decrease towards the periphery, so that sensitivity to shearing motion is minimal near the border of the stimulus. In this way, sensitivity is greater when a square wave is positioned with the motion boundary at the fixation point than when the motion boundary is further in the periphery.

In this model, where the sizes of the receptive fields increased linearly [equations (5) and (6)] the increase with eccentricity is quite dramatic: for example, σ_c is

about 50 times greater at the edge of the stimulus than at the center for observer WLS. In a different version of the model we allowed the size to increase as a logarithmic function which added a parameter that determined the curvature of the function relating size to eccentricity, allowing size to increase more near the center than the periphery. With that additional degree of freedom, σ_c was about 40 times greater at the edge of the stimulus than at the center, but the improvement of fit was negligible.

In order to test the importance of independent size scaling for center and surround, we ran a simulation for the case in which the sizes were scaled at the same rate with eccentricity, i.e. the ratio of the sizes of center and surround was kept constant. If the sizes of the receptive fields increase by the same factor, then sensitivity to motion boundaries cannot decrease to zero with eccentricity. With this constraint, the model failed to capture the empirical difference in sensitivity to square waves in even vs odd phase. In fact, the simulated sensitivity was greater for the square wave in even phase than in odd phase for frequency f1. In odd phase, the stimulus contains three motion boundaries, two at the edges and one at the fixation point. The square wave stimulus in even phase has four motion boundaries, two at the edges and one on either side of the fixation point. If the sensitivity to motion boundaries is not scaled down with eccentricity, the additional motion boundary in the even phase leads to the wrong prediction. Any successful model will therefore have to assign greater sensitivity to shearing motion at the center of the visual field than in the periphery.

Density or sensitivity of shear sensors

One way to assign greater importance to the detectors at the center is to stipulate that there are more of them per unit area than in the periphery. In that way, a stimulus in the center will elicit responses from a greater number of units, all of which contribute to detection by probability summation. In the psychometric function this can be simulated as:

$$P_{\text{detect}} = 1 - \prod_{j=1}^{110} [1 - (1 - 2^{-(\text{DOG}_j/\beta)^x})]^{\text{density}(j)}, \quad (10)$$

where $\text{density} \geq 1$. The function for density (j) is thus used to increase the number of identical responses at any location j . We used a two-parameter power function which allowed a non-linear change in density with eccentricity. The values of density (j) are equal to 1.0 for the edge units 1 and 110 and increase towards the center, being highest at the fixation point. A density function can find justification in a system of receptive fields whose sizes increase with eccentricity because fewer receptive fields are needed in the periphery to provide the same degree of coverage. Similar properties have been proposed for mechanisms in the luminance domain (Rovamo & Virsu, 1979; Wilson & Bergen, 1979; Watson, 1983). The density value can also be interpreted as a factor by which the response of a unit is weighted. In equation (10) density (j) can be

pulled inside the exponent, where it operates as a factor multiplying the response of each unit. This parameter effectively reduces the sensitivity of shear detectors in the periphery.

We tested the performance of the model with the added density (j) function for the case where the scaling factors of the center and surround were yoked together. With the addition of the density (j) function, the fit of the yoked-size model to the data was as good as, and practically indistinguishable from, that of the model with independent size scaling. The diameter of receptive fields at the edge of the stimulus was only 14 times larger than at the center in this case. On the other hand, the postulated receptor density for the best fit was more than 20,000 times greater in the center than in the periphery. It seems that a tradeoff is possible between density and scaling parameters while retaining a good fit to the data.

We were also interested in seeing what would happen with independent size scaling of center and surround regions in the standard model when the density function was added. The fit to the data was, of course, at least as good as before, but not perceptibly better. The sizes of center and surround regions providing optimum fit to the data are shown in Fig. 17(a, b) for observers WLS and AI. Locations of the weighting functions are shown on the abscissa, and the sizes on the ordinate. Surround units, shown as dashed lines, are always larger than center units, shown as solid lines. The ratios of surround and center are shown in Fig. 17(c) for both observers. Ratios are > 1.0 for both observers, indicating that shear sensors at all eccentricities respond well to shearing stimuli. Figure 17(d) shows values of density (j) for both observers. For observer AI, sensitivity is almost 20,000 times greater at the fixation point than in the periphery. For observer WLS, periphery and fixation point differ by a factor of more than 2000.

In the standard model without the density function, decreased sensitivity in the periphery was achieved by making the sizes of the center and surround regions similar. Sensitivity can also be controlled by a density function. Factors determining sensitivity can thus be traded off against each other, as in the case of the relative sizes of the subunits and the density functions.

First derivative of Gaussian receptive fields

Another receptive field structure that would respond well to shearing motion is the derivative of a Gaussian. This receptive field possesses two lobes of opposing signs, so that response to a field of uniform motion is zero. Only one set of parameters is needed to scale the size of the receptive field. Larger fields, though, are not necessarily less sensitive to shearing motion than small receptive fields. We modeled the performance of such a system of receptive fields based on the derivative of a Gaussian whose sizes increased with eccentricity, and found that performance was not as good as with the difference of Gaussians. In particular, sensitivity to square waves in even phase was greater than for the odd phase, which was the opposite of the experimen-

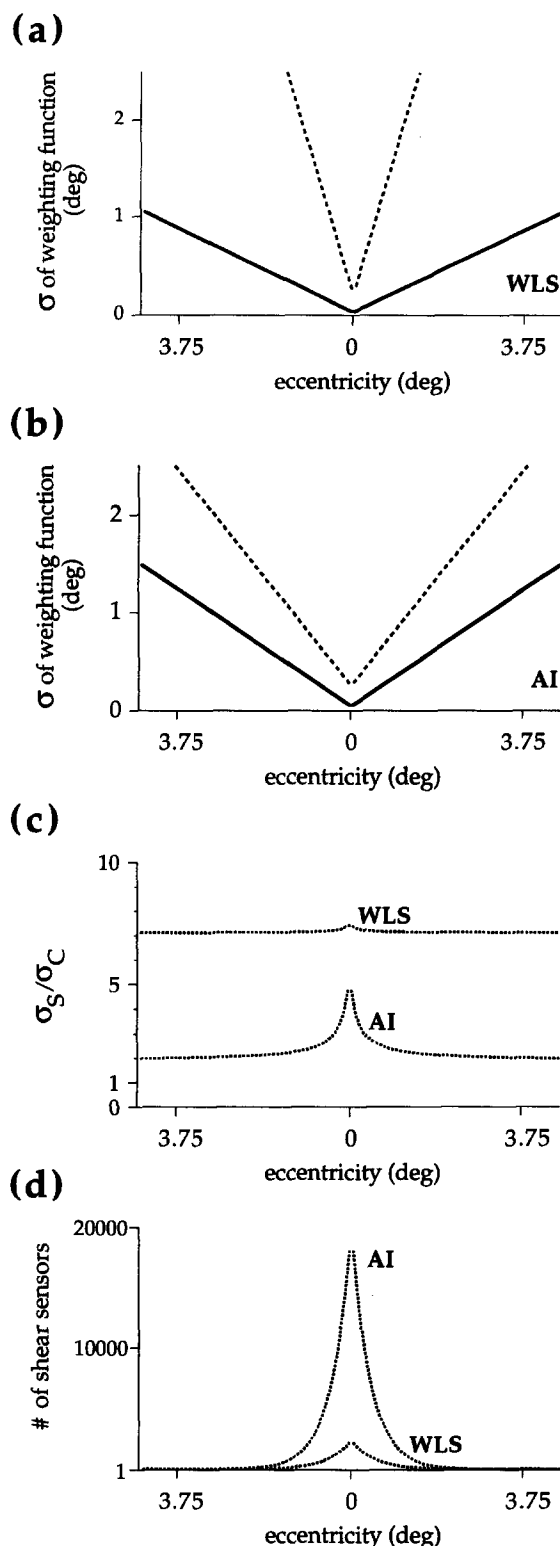


FIGURE 17. (a) Sizes of center and surround subunits at different eccentricities for model incorporating parameters for the density of shear sensors at each location. Sizes are shown for parameter settings giving the best fit to experimental results of observer WLS. Solid and dotted lines show sizes of center and surround subunits, respectively, as a function of eccentricity. The ordinate gives the SD of each subunit. At the fixation point, $\sigma_c = 0.037$ deg, $\sigma_s = 0.272$ deg. For details, see Fig. 16. (b) Sizes of subunits at different eccentricities for model fit to data of observer AI. At the fixation point, $\sigma_c = 0.059$ deg, $\sigma_s = 0.278$ deg. (c) Ratio of size of surround to size of center subunits for the two observers. (d) Density of shear sensors for the two observers, given as the number of identical mechanisms generating identical responses at each location. A greater number of mechanisms corresponds to a greater contribution to detection of the stimulus.

tal results. Since sensitivity to shearing motion did not decrease markedly with eccentricity in this model, sensitivity for the stimulus with the greater number of motion boundaries prevailed.

This problem could be dealt with by introducing the density function discussed earlier. In this way, sensitivity to shearing motion was greatest at the fixation point, and declined towards the periphery. With this additional property, the model with a derivative of Gaussian receptive field profile captured the properties of the data. Performance was comparable to the difference of Gaussians model.

It seems, then, that a number of receptive field structures will perform adequately to explain the data, provided they incorporate the key properties of sensitivity to shearing motion, size scaling with eccentricity, and a decrease in density or sensitivity in the periphery.

Simple loss of sensitivity in the periphery cannot substitute for size scaling. We tested the model incorporating the derivative of a Gaussian receptive field profile without size scaling but with a decrease of sensitivity in the periphery. For the best fit, there were a number of mismatches between data and model. In particular, the model showed too high a sensitivity to flutes at f_3 and f_9 as well as square waves at f_9 , while sensitivity was too low for sine waves at f_1 and f_3 . That is, the effects of the change in the preferred frequency range that comes with size scaling cannot be simulated with a simple loss of sensitivity in the periphery.

Gaussian receptive fields

For completeness we tested a simple Gaussian weighting function, i.e. a unit that pools motion responses in one direction without an opposed region. Not surprisingly, this model categorically failed to match the data. The lack of an inhibitory surround makes for a lowpass response spectrum for sine waves, while the results shown in Fig. 6 exhibit a bandpass relationship between spatial frequency and sensitivity. Furthermore, since the simple Gaussian receptive field does not give a strong response to motion boundaries, responses to square waves in different phases were practically identical, unlike the experimental data. The Gaussian weighting function will in fact blur motion boundaries. The information that is lost in that way is apparently critical for the performance of the visual system.

SUMMARY OF MODELING RESULTS

Experimental results on the detection of shearing motion show a greater sensitivity for stimuli with sharp motion boundaries than for shallower velocity gradients. Sensitivity decreases when motion boundaries are not at the fixation point. In addition, experiments with fluted waveforms showed that large areas of uniform motion are not critical in determining sensitivity to motion when motion boundaries are located at the fixation point. These properties of the data could

be captured by a model of opponent center-surround units that sum responses of motion-sensing units. The general properties of the model are based on the following:

- (a) linear opponent regions sampling the velocity domain;
- (b) size-scaling with eccentricity;
- (c) decrease in density or sensitivity with eccentricity.

We tested two different versions of this model, one with a difference of Gaussians arrangement, the other based on the derivative of a Gaussian, and results were very similar. Models that did not possess the three properties listed above failed to perform adequately.

The model with linear opponent regions explains the results for square and sinusoidal waves at different frequencies shown in Fig. 6. The points shown are the 80% detection probabilities for the empirical psychometric curves, which were fit very precisely by the model (Figs 14 and 15). Therefore, the model exhibits the same bandpass characteristics for sine waves and the low-pass function for square waves as in Fig. 6. For frequencies below 1.2 c/deg, thresholds increase for sine waves but remain constant for square waves in odd phase. In the model, sensitivity to sharp velocity gradients is highest at the center, and decreases towards the periphery. As long as a motion boundary is located at the fixation point, sensitivity will remain largely unaffected by decreasing frequency of the square wave. For the sine wave, on the other hand, the velocity gradient decreases with decreasing frequency, so that sensitivity is expected to decrease. Units in the periphery may be more sensitive to the lower frequencies than units in the center, but since they are also less sensitive overall, they contribute less to detection.

These modeling results show that complex data on sensitivity to shearing motion can be explained by relatively simple processes. The results suggest that steep velocity gradients play an important role in the processing of motion information, and that computational models making use of that information could help segment images.

REFERENCES

- Adelson, E. H. & Bergen, J. R. (1985). Spatiotemporal energy models for the perception of motion. *Journal of the Optical Society of America A*, 2, 284-299.
- Banton, T. & Levi, D. M. (1993). Spatial localization of motion-defined and luminance-defined contours. *Vision Research*, 33, 2225-2237.
- Bergen, J. R., Burt, P. J., Hingorani, R. & Peleg, S. (1990). Multiple component image motion: Motion estimation. David Sarnoff Research Center Technical Report.
- Black, M. J. & Anandan, P. (1993). A framework for the robust estimation of optical flow. In *Proceedings International Conference on Computer Vision, ICCV 1993* (pp. 231-236). Washington, D.C.: Computer Society Press of the IEEE.
- Clocksink, W. F. (1980). Perception of surface slant and edge labels from optical flow: A computational approach. *Perception*, 9, 253-269.

- van Doorn, A. J. & Koenderink, J. J. (1982). Visibility of movement gradients. *Biological Cybernetics*, *44*, 167-175.
- van Doorn, A. J. & Koenderink, J. J. (1983). Detectability of velocity gradients in moving random-dot patterns. *Vision Research*, *23*, 799-804.
- Fennema, C. L. & Thompson, W. B. (1979). Velocity discrimination in scenes containing several moving objects. *Computer Graphics and Image Processing*, *9*, 301-315.
- Golomb, B., Andersen, R. A., Nakayama, K., MacLeod, D. I. A. & Wong, A. (1985). Visual thresholds for shearing motion in monkey and man. *Vision Research*, *25*, 813-820.
- Graham, C. H., Baker, C. E., Hecht, M. & Lloyd, V. V. (1948). Factors influencing thresholds for monocular movement parallax. *Journal of Experimental Psychology*, *38*, 205-223.
- Hawken, M. J., Gegenfurtner, K. R. & Tang, C. (1994). Contrast dependence of colour and luminance motion mechanisms in human vision. *Nature*, *367*, 268-270.
- von Helmholtz, H. (1925). *Helmholtz's treatise on physiological optics* (Vol. III) (translated Southall, J. P. from the third German edition edn). Washington, D.C.: Optical Society of America.
- Hoel, P., Port, S. & Stone, C. (1971). *Introduction to statistical theory*. Boston, Mass.: Houghton Mifflin.
- Hoffman, D. D. (1982). Inferring local surface orientation from motion fields. *Journal of the Optical Society of America A*, *72*, 888-892.
- Horn, B. K. P. & Schunck, B. G. (1981). Determining optical flow. *Artificial Intelligence*, *17*, 185-203.
- Hutchinson, J., Koch, C., Luo, J. & Mead, C. (1988). Computing motion using analog and binary resistive networks. *Computer, March*, 52-63.
- Kaplan, G. A. (1969). Kinetic disruption of optical texture: The perception of depth at an edge. *Perception & Psychophysics*, *6*, 193-198.
- Koenderink, J. J. & van Doorn, A. J. (1975). Invariant properties of the motion parallax field due to the movement of rigid bodies relative to an observer. *Optica Acta*, *22*, 773-791.
- Koenderink, J. J. & van Doorn, A. J. (1976). Local structure of movement parallax of the plane. *Journal of the Optical Society of America A*, *66*, 717-723.
- Koenderink, J. J. & van Doorn, A. J. (1992). Second-order optical flow. *Journal of the Optical Society of America A*, *9*, 530-538.
- Lenert, L. H. (1970). *Advanced technical mathematics*. Columbus, Ohio: Charles E. Merrill.
- Longuet-Higgins & Prazdny, K. (1980). The interpretation of a moving retinal image. *Proceedings of the Royal Society of London B*, *208*, 385-397.
- Mumford, D. & Shah, J. (1989). Optimal approximations by piecewise smooth functions and associated variational problems. *Communications of Pure & Applied Mathematics*, *42*, 577-685.
- Murray, D. W. & Buxton, B. F. (1987). Scene segmentation from visual motion using global optimization. *IEEE Transactions on Pattern Analysis and Machine Intelligence PAMI-9*, 220-228.
- Nakayama, K. (1981). Differential motion hyperacuity under conditions of common image motion. *Vision Research*, *21*, 1475-1482.
- Nakayama, K. & Loomis, J. M. (1974). Optical velocity patterns, velocity-sensitive neurons, and space perception: A hypothesis. *Perception*, *3*, 63-80.
- Nakayama, K. & Tyler, C. W. (1981). Psychophysical isolation of movement sensitivity by removal of familiar position cues. *Vision Research*, *21*, 427-433.
- Nakayama, K., Silverman, G. H., MacLeod, D. I. A. & Mulligan, J. (1985). Sensitivity to shearing and compressive motion in random dots. *Perception*, *14*, 225-238.
- Nelder, J. A. & Mead, R. (1965). *Computer Journal*, *7*, 308-313.
- Nesi, P. (1993). Variational approach to optical flow estimation managing discontinuities. *Image & Vision Computing*, *11*, 419-439.
- Quick, R. F. Jr (1974). A vector-magnitude model of contrast detection. *Kybernetik*, *16*, 65-67.
- Ratliff, F. (1965). *Mach bands: Quantitative studies on neural networks in the retina*. San Francisco, Calif.: Holden-Day.
- Regan, D. (1986). Form from motion parallax and form from luminance contrast: Vernier discrimination. *Spatial Vision*, *1*, 305-318.
- Reichardt, W. (1961). Autocorrelation, a principle for the evaluation of sensory information by the central nervous system. In Rosenblith, W. A. (Ed), *Sensory communication* (pp. 303-317). Cambridge, Mass.: MIT Press.
- Rogers, B. & Graham, M. (1979). Motion parallax as an independent cue for depth perception. *Perception*, *8*, 125-134.
- Rovamo, J. & Virsu, V. (1979). An estimation and application of the human cortical magnification factor. *Experimental Brain Research*, *37*, 495-510.
- Sachtler, W. L. & Zaidi, Q. (1990). Motion detection and the role of motion boundaries. *Investigative Ophthalmology and Visual Science (Suppl.)*, *31*, 512.
- Sachtler, W. L. & Zaidi, Q. (1993). Effect of spatial configuration on motion aftereffects. *Journal of the Optical Society of America A*, *10*, 1433-1449.
- Sachtler, W. L. & Zaidi, Q. (1994). Visual processing of simple and multiple motion components. *Spatial Vision*. Submitted.
- van Santen, J. P. H. & Sperling, G. (1985). Elaborated Reichardt detectors. *Journal of the Optical Society of America A*, *2*, 300-321.
- Shulman, D. & Hervé, J.-Y. (1989). Regularization of discontinuous flow fields. In *Proceedings of the Workshop on Visual Motion* (pp. 81-86). Washington, D.C.: IEEE Computer Society Press.
- Singh, A. & Allen, P. (1992). Image-flow computation: An estimation-theoretic framework and a unified perspective. *Computer Vision, Graphics, and Image Processing: Image Understanding*, *56*, 152-177.
- Snowden, R. J. (1992). Sensitivity to relative and absolute motion. *Perception*, *21*, 563-568.
- Thompson, P. (1982). Perceived rate of movement depends on contrast. *Vision Research*, *22*, 377-380.
- Ullman, S. (1979). *The interpretation of visual motion*. Cambridge, Mass.: MIT Press.
- Watamaniuk, S. N. J., Sekuler, R. & Williams, D. W. (1989). Direction perception in complex dynamic displays: The integration of direction information. *Vision Research*, *29*, 47-59.
- Watson, A. B. (1979). Probability summation over time. *Vision Research*, *19*, 515-522.
- Watson, A. B. (1983). Detection and recognition of simple spatial forms. In Braddick, O. J. & Sleigh, A. C. (Eds), *Physical and biological processing of images* (pp. 100-114). New York: Springer.
- Watson, A. B. (1986). Temporal sensitivity. In Boff, K. R., Kaufman, L. & Thomas, J. P. (Eds), *Handbook of perception and human performance* (Vol. I). New York: Wiley.
- Watson, A. B. & Ahumada, A. J. Jr (1985). Model of human visual-motion sensing. *Journal of the Optical Society of America A*, *2*, 322-342.
- Watson, A. B. & Eckert, M. P. (1994). Motion-contrast sensitivity: Visibility of motion gradients of various spatial frequencies. *Journal of the Optical Society of America A*, *11*, 496-505.
- Westheimer, G. (1954). Eye movement responses to a horizontally moving visual stimulus. *Archives of Ophthalmology (Chicago)*, *52*, 932-941.
- Wilson, H. R. & Bergen, J. R. (1979). A four mechanism model for threshold spatial vision. *Vision Research*, *19*, 19-32.
- Zaidi, Q. & Sachtler, W. L. (1992). Motion adaptation from surrounding stimuli. *Perception*, *20*, 703-714.

Acknowledgements—We wish to thank Terry Boulton, Charlie Chubb, Len Matin, and Warren Meck for comments on an earlier version of this paper, and Alla Igelnik for patient and careful observation. This research was partially supported by the National Eye Institute through grant EY07556 to Q. Zaidi.